Review article

Jolly Xavier[a], Serge Vincent[a], Fabian Meder[a] and Frank Vollmer[a,*]

Advances in optoplasmonic sensors – combining optical nano/microcavities and photonic crystals with plasmonic nanostructures and nanoparticles

https://doi.org/10.1515/nanoph-2017-0064
Received June 16, 2017; revised August 10, 2017; accepted August 18, 2017

Abstract: Nanophotonic device building blocks, such as optical nano/microcavities and plasmonic nanostructures, lie at the forefront of sensing and spectrometry of trace biological and chemical substances. A new class of nanophotonic architecture has emerged by combining optically resonant dielectric nano/microcavities with plasmonically resonant metal nanostructures to enable detection at the nanoscale with extraordinary sensitivity. Initial demonstrations include single-molecule detection and even single-ion sensing. The coupled photonic-plasmonic resonator system promises a leap forward in the nanoscale analysis of physical, chemical, and biological entities. These optoplasmonic sensor structures could be the centrepiece of miniaturised analytical laboratories, on a chip, with detection capabilities that are beyond the current state of the art. In this paper, we review this burgeoning field of optoplasmonic biosensors. We first focus on the state of the art in nanoplasmonic sensor structures, high quality factor optical microcavities, and photonic crystals separately before proceeding to an outline of the most recent advances in hybrid sensor systems. We discuss the physics of this modality in brief and each of its underlying parts, then the prospects as well as challenges when integrating dielectric nano/microcavities with metal nanostructures. In Section 5, we hint to possible future applications of optoplasmonic sensing platforms which offer many degrees of freedom towards biomedical diagnostics at the level of single molecules.

Keywords: label-free biosensors; optoplasmonics; optical microcavity; plasmonics; photonic crystal; whispering-gallery mode.

1 Introduction

Optical nano/microcavities are nano/microstructures that confine light for extended periods of time, resulting in optical resonances that can exhibit very narrow linewidths and high quality factors (i.e. Q-factors). The quality factor can be plainly expressed as $Q=\omega_{\mathrm{Res}}\tau$ where ω_{Res} is the resonant angular frequency and τ is the ring-down lifetime. Sensors that use these elements are subject to strong light-matter interactions as light encounters an analyte upon each cavity pass, thus elevating the sensitivity. A whispering-gallery mode (WGM) cavity, such as a glass microsphere, is an example of this wherein light can be trapped due to total internal reflection. The number of round trips in such a cavity is limited by absorption, radiation, scattering, and other forms of loss. The Q-factor characterises these losses, as it also describes the fraction of energy lost per cycle. When continuously pumped, light will interfere with itself every round trip and set up an optical resonance with a Lorentzian line shape. In the simplest case, a collection of biomolecules binding to a microspherical cavity will result in a resonant wavelength shift $\Delta\lambda_{\mathrm{Res}}=\lambda\sigma\alpha_{\mathrm{Ex}}/[\epsilon_0(n_s^2-n_m^2)R]$ where σ is the surface density of bound biomolecules, α_{Ex} is the polarisability of biomolecules in excess of the external medium (e.g. water), n_s and n_m are, respectively the sphere and external medium refractive indices, and R is the microsphere radius [1, 2]. Q-factors of 10^{6-7} are common in biosensing applications [3] and the aim is to

[a]**Jolly Xavier, Serge Vincent, Fabian Meder and Frank Vollmer:** These authors contributed equally to this work.
***Corresponding author: Frank Vollmer,** Living Systems Institute, Department of Physics and Astronomy, University of Exeter, EX4 4QD, Exeter, UK; and Max Planck Institute for the Science of Light, Staudtstr. 2, D-91058 Erlangen, Germany, e-mail: f.vollmer@exeter.ac.uk.
http://orcid.org/0000-0003-0565-4671
Jolly Xavier and Serge Vincent: Living Systems Institute, Department of Physics and Astronomy, University of Exeter, EX4 4QD, Exeter, UK; and Max Planck Institute for the Science of Light, Staudtstr. 2, D-91058 Erlangen, Germany
Fabian Meder: Max Planck Institute for the Science of Light, Staudtstr. 2, D-91058 Erlangen, Germany; and Center for Micro-BioRobotics, Italian Institute of Technology, Viale Rinaldo Piaggio, 34, 56025 Pontedera, Italy

optimise the Q while further reducing the mode volume $V = \int \epsilon |\boldsymbol{E}(\boldsymbol{r})|^2 dV / \max[\epsilon |\boldsymbol{E}(\boldsymbol{r})|^2]$, where ϵ is the permittivity and $\boldsymbol{E}(\boldsymbol{r})$ is the position-dependent electric field [4].

Plasmonic nanostructures and nanoparticles, on the other hand, confine light to nanoscale modal volumes V where even modest Q-factors (e.g. 10–100) of localised surface plasmon resonances (LSPRs) can result in very high near-field intensity enhancements. Such sensors have resonance shifts similar to those of optical nano/microcavities [5–7], where factors influencing the shift include the molecule's polarisibility, the modal volume, and the locally enhanced field at a "hot spot". The enhancement can strongly vary between plasmonic nanostructure geometries and, furthermore, explicit formulas for the resonance shift of plasmonic nanocavities by single nanoparticles or biomolecules have been derived [8, 9].

Sensing with high-Q optical nano/microcavities and plasmonic nanoparticles has been studied extensively for detecting physical, chemical, and biological entities. Specificity in detection is often carried out with receptor molecules that establish analyte-specific interaction kinetics, traceable vis-à-vis perturbations in the optical or plasmonic resonances involved. Over the last decade, the underlying photonic and plasmonic sensing technologies have been dramatically improved. Most recently, both sensor structures have been combined into optoplasmonic systems as to simultaneously benefit from high Q-factors, small modal volumes, and extreme near-field enhancements. A compromise between loss and field enhancement/confinement has to be sought in such a way as to viably increase Q/V and raise the field intensity at the sensing site. As such, photonic-plasmonic hybdrisation lays the foundation for novel device physics, sensing modalities, and unprecedented detection limits, with demonstrations that include single-molecule and single-ion sensing.

This review is intended for the specialist in the areas of photonics or plasmonics who may not have been exposed to the emerging field of optoplasmonic sensor systems. These hybrid systems originate from three different fields: nanoplasmonics, high-Q WGM microcavities, and photonic crystals (PhCs). To convey the interdisciplinarity, it is instructive to first review current advances in the underpinning technologies separately. After the state of the art for sensing with plasmonic nanostructures and high-Q optical WGM microcavities are covered, a comprehensive review of the nascent field of optoplasmonic sensors follows. A discussion of one of the very promising means for integrating high-Q optical nano/microcavities and nanoplasmonic systems onto PhC devices follows. The most recent integration efforts for potential applications, e.g. analytical platforms, are highlighted. The review closes with a discussion and outlook on the unique opportunities for sensing with plasmon-enhanced optical nano/microcavities within a chip-scale package.

2 Plasmonic nanoparticles and nanostructures

Plasmonic nanoparticles and nanostructures, with dimensions smaller than the wavelength of incident light, are well known to confine light and enhance its interaction with matter. In what is typically noble metal nanoparticles (e.g. gold, silver, palladium, etc.), an incident light beam induces a collective oscillation of conduction band electrons depending on the nanoparticle size, shape, and composition. These electron oscillations in the plasmonic nanostructures are confined to nanoscale volumes, depicted in Figure 1 and under what is termed a LSPR, leading to enhanced and highly localised electromagnetic fields that are several orders of magnitude stronger than the incident field – different from propagating surface plasmons on a planar, extended metallic surface [12–14]. In view of this resonant behaviour, plasmonic nanoparticles and nanostructures act as independent sensor

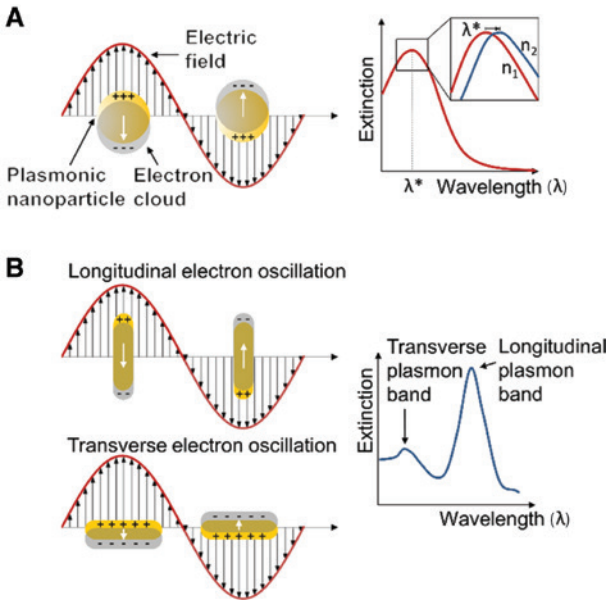

Figure 1: LSPR excitation and extinction spectra for plasmonic (A) nanoparticles and (B) nanorods.
LSPR sensors detect shifts in the resonance wavelength λ^*, shown in the extinction spectra of (A), in response to alterations in the refractive index of the medium containing the plasmonic nanoparticle. The nanorods of (B) show longitudinal and transverse plasmon bands corresponding to the electron oscillations along the long and short axes, respectively. Adapted and modified from [10, 11].

elements that strongly improve surface plasmon-based sensing [7, 12, 15–17]. The LSPR depends on the size and morphology of the nanoparticles and the electromagnetic field is concentrated in local features such as tips or edges, generating focused hot spots with sizes similar to single molecules (e.g. the nanorod's dipole pattern in Figure 1B).

LSPRs are particularly interesting for sensing applications as the resonant frequency of the oscillating plasmons depends on the changing dielectric properties of the local medium (i.e. effective refractive index change) within the decay length of the electromagnetic field [15]. The change in chemical and molecular properties at the hot spots (for example, by adsorption of molecules) or in hybridised electromagnetic fields of nearby plasmonic nanoparticles can be sensitively measured by observing plasmon resonance variations [5, 13, 18, 19]. There is a shift in the resonant wavelength λ^* in response to an alteration in the refractive index of the medium containing the plasmonic substance (see the inset of Figure 1A) [10]. The sensitivity can be calculated to be $S_n = d\lambda^*/dn = (d\epsilon_r^*/dn)/(d\epsilon_r/d\lambda)_{\lambda^*} = -2\chi n/(d\epsilon_r/d\lambda)_{\lambda^*}$, where the resonance condition for the real part of the plasmonic substance's dielectric function is $\epsilon_r^* = \epsilon_r(\lambda^*) = -\chi n^2$ and the factor χ puts shape into account (i.e. $\chi = 2$ for spheres) [10, 11]. Judicious choice of morphology and material hence allows for optimisation of the magnitude of λ^* with n, strategies for which are discussed in the next section of this review. A LSPR is virtually sensitive to all molecules interacting within hot spots; therefore, specificity comes from the surface chemistry of the resonator (e.g. via antibodies to detect antigens). A further important consequence of the enhanced, localised fields is the several orders of magnitude increased emission and/or scattering signals from the adsorbed molecules leading to a surface-enhanced fluorescence effect and surface-enhanced Raman scattering (SERS) [15, 18, 20, 21]. Here, we will focus on a selection of recent developments in the synthesis of plasmonic nanostructures, fine-tuning of the electromagnetic field localisation, and enhancements at specific sites, tailored surface functionalisation, and their resulting properties. For a rigorous treatment of surface plasmons, we refer the reader to [7, 12, 15–17, 22].

2.1 Diverse plasmonic nanoparticles and nanostructures with tailored geometries and sensing properties

Plasmonic sensors can be accurately tuned towards excitation sources, the analyte, the analyte's environment, and the overall platform by resonant coupling or controlled nanostructuring/sizing. In the last few years, synthetic approaches to shape nanoparticles and nanostructures in wet chemical synthesis and electron or ion beam lithography have drastically matured and led to a great diversity of probable plasmonic structures with tuneable resonances. Wet chemical synthetic methods advanced in terms of size and shape homogeneity, with complex shapes such as spheres, stars, triangles, core-shell particles, hollow boxes, etc. (Figure 2). It follows that "traditional" spherical or rod-shaped nanoparticles used for plasmonic sensing applications are supplemented rather than replaced by particles with more complex shapes that confer specific advantages. Figure 2A shows the dramatic effect of a slight elongation of a spherical particle into a rod-like particle on the scattering spectrum [23]. The elongation alone strongly improves refractive index sensing sensitivity and, due to their straightforward geometry and synthesis, gold nanorods are widely used in plasmonic sensing [12, 35]. Complex structuring not only provides the opportunity to tune the plasmon resonance frequencies to certain wavelengths but to refine the size, number, and location of hot spots on a single particle and tailor the system for the desired applications. This is because the electron oscillation is localised along the axes or at the edges and corners of non-spherical nanoparticles (or both), leading to an additional shape-dependent depolarisation and splitting of the surface plasmon resonance (SPR) into several modes, such as longitudinal and transverse modes for nanorods or symmetric and antisymmetric modes in nanoshells (Figure 2F shows a Au nanoshell obtained by Au coating of a SiO_2 core) [18]. Figure 2B–G gives examples of particle shapes, wherein others can be found in a "periodic table" of plasmonic structures published by Tan et al. [13]. Triangles and symmetric stars, for example, contain defined edge- and tip-engineered plasmon hot spots leading to enhanced SERS sensitivity granted by symmetry and local field enhancements (Figure 2C and E) [24, 25]. Galvanic replacement reactions allow one to obtain hollow Au-Ag structures with plasmon resonances depending on the chemical conversion during the replacement reaction (Figure 2D) [26, 36]. Symmetric nanoscale surface features which create plasmonic hot spots also exist, in terms of structural appearance, in protein capsids of natural nanoparticles such as viruses. In a reproduction of virus shapes, plasmonic nanoparticles were obtained with a 10^6 higher sensitivity as compared to spheres with tuneable hot spots and, for the future, their biological counterparts for sensing molecules intracellularly (Figure 2H) [29].

LSPR sensors based on such highly symmetric nanoparticles generally operate independently of the

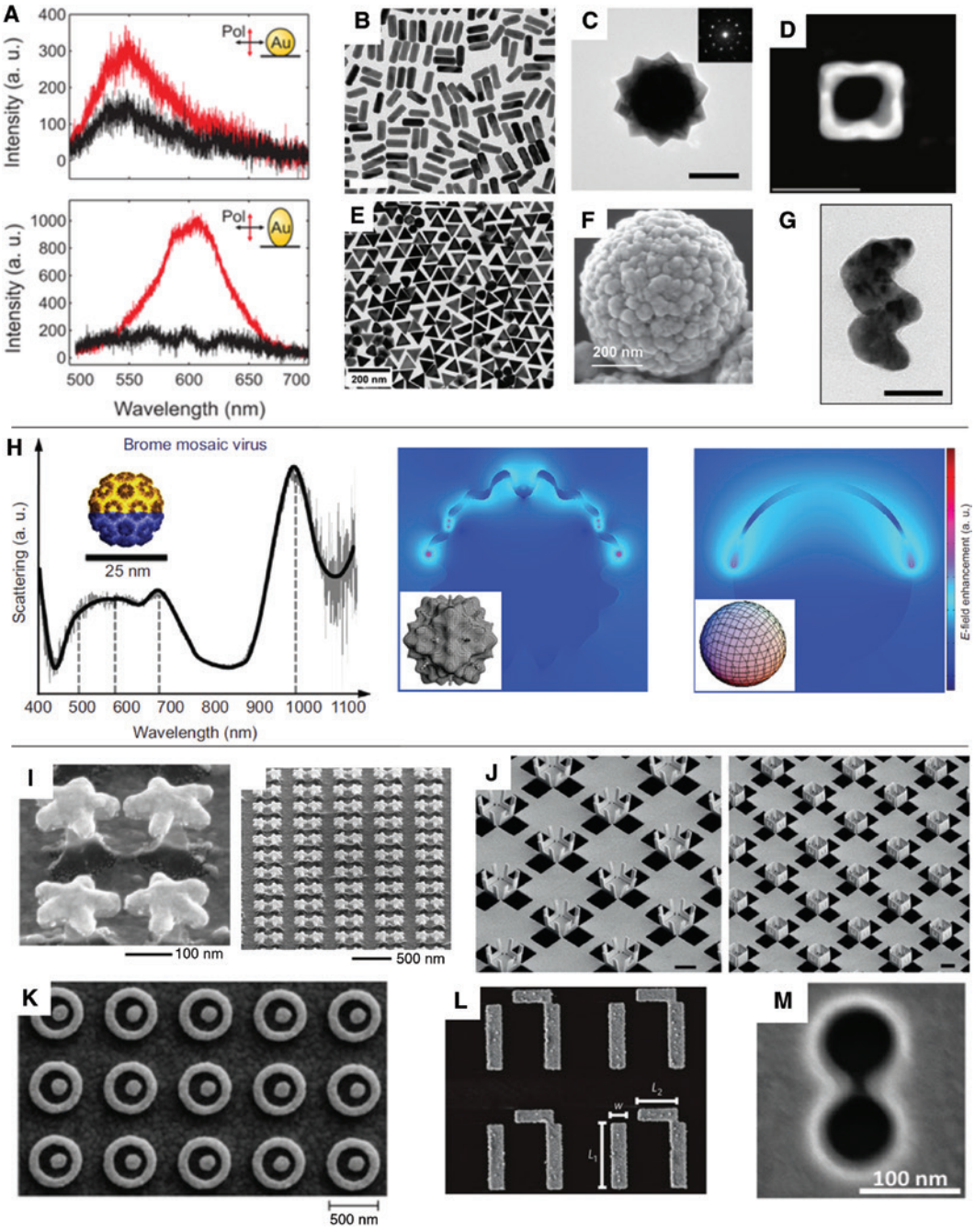

Figure 2: Shape and properties of plasmonic nanostructures.
(A) Scattering spectra under linearly polarised dark-field excitation for a spherical 80-nm gold nanoparticle (upper panel) and elongated particle after melting the spherical particle to 110 nm × 68 nm (lower panel). The polarisation of the white excitation light is perpendicular (red curves) or parallel (black curves) to the glass coverslip. Adapted from [23]. (B)–(G) Transmission electron microscopy (TEM) and scanning electron microscopy (SEM) images of differently shaped Au-based plasmonic nanoparticles, with scale bars of 100, 100, 50, 200, 200, and 50 nm, respectively. Adapted from [23–28]. (H) "Bioinspired" surface structuring of plasmonic particles. The left panel is a scattering spectrum of a Brome mosaic virus coated with a 5-nm gold layer (i.e. via metal evaporation), while the two right panels are simulated electromagnetic field enhancement distributions of a gold-coated virus and a gold-conjugated nanosphere. The virus capsid morphology generates more optically enhanced spots than the sphere. Adapted from [29]. (I) SEM images at a 52° tilted view of the Au nanostar on Si pillar dimers with a 6-nm interparticle spacing and a 150-nm Si pillar height. Adapted from [30]. (J) SEM images of ion-beam irradiation-induced folded in-plane Au boxes with U-shaped walls (left) and boxes with U-shaped holes on the walls (right). Scale bars are 1 μm. Adapted from [31]. (K) SEM image of asymmetric ring/disk Au nanostructure with Fano-type resonances. Adapted from [32]. (L) SEM image of a Au-based plasmonic Fano-resonant asymmetric metamaterial used for detecting biorecognition reactions and biomolecule orientations. $L_1 = 1.8$ μm, $L_2 = 0.9$ μm, and $w = 0.36$ μm. Adapted from [33]. (M) SEM image of a Au double nanohole used to trap and sense single biomolecules. Adapted from [34].

polarisation of the incident light. Specific shapes such as that in Figure 2G, however, lead to natural chirality [11, 37]. This enables LSPRs that are detectable via circular dichroism spectra, which are typically more feature-rich than extinction spectra and can be used for sensing more spectral signatures in complex biological systems with maximised sensitivity [11]. Coupling and bridging single nanoparticles and the creation of dimers with controlled gap distances establishes constructive coupling between plasmon resonances of adjacent nanoparticles and regions of intense local fields in the gaps between the nanoparticles. The local field enhancements facilitate single-molecule resolution in SERS and dark-field microscopy, where the gap width can be precisely set, e.g. by self-assembled monolayers of surface molecules or DNA-assisted coupling tethering of the nanoparticles [14, 19, 38–42].

Electron and ion beam structuring is another tool to generate plasmonic structures on various substrates with highly reproducible structural shape and electromagnetic field enhancements [30, 43]. Figure 2I shows an example in which star-shaped dimers are generated to couple and enhance the fields in sub-10-nm gaps between the nearby tips. By elevating the stars, the field is additionally decoupled from the underlying substrate [30]. This prearrangement leads to an enhancement of the Raman scattering of about 10^7 in addition to an enhancement originating from the individual nanostructures sufficient to detect single adenine molecules [30]. Similar effects provide, for example, Au nanotriangles coupled at their tips or coupled with spheres [19]. Resonant coupling is determined by the shape and distance between two vicinal nanostructures. If the interference between a spectrally overlapping broad resonance or continuum and a narrow discrete resonance occurs, the fundamental criterion for Fano resonances is fulfilled [44]. Structures such as complex three-dimensional geometries or simpler ring/disk cavities for generating Fano resonances are shown in Figure 2J–L, which are (among other applications) very interesting for sensing purposes [31–33, 44]. Molecules that adsorb onto a Fano-resonant structure can induce a notably large spectral shift in the resonance frequency due to resonant coupling, which creates enhanced sensing capabilities [31–33, 44]. Quite often, only binding events are sensed and no conformational information of the interacting molecules is recovered. An array of infrared plasmonic Fano-resonant asymmetric metamaterials (FRAMMs) shown in Figure 2L, however, enabled structure-resolving label-free probing of binding characteristics of recognition proteins and, simultaneously, gave information on their surface orientation using biomolecular characteristic mid-infrared vibrational fingerprints [33].

Interesting and promising features for biosensing were also shown for optical traps such as double nanohole structures (Figure 2M) [34, 45–49]. The specific structure of the double nanoholes results in an optical tweezer that can trap and simultaneously sense single biomolecules in a label-free manner [46]. This particular trap may be combined with measurements of Raman-active acoustic modes to obtain specific information on single nanoparticles and biomolecules [47] or to control translocation of biomolecules through the trap via switching the plasmonic field, e.g. for controlled DNA sequencing [49].

2.2 New plasmonic material combinations

The material for a plasmonic nanostructure or nanoparticle is yet another parameter to fine-tune excitation as well as detection sensitivity/selectivity, usually restricted to materials with strong plasmonic coupling like Au or Ag. The material dispersion function, a key factor in the sensitivity of LSPR nanosensors, has thus been limited to the dielectric functions of those pure metals [11]. It is suggested that sensitivity can be improved by reducing the wavelength dependence of the real part of the material dielectric function [11]. This was shown for different doping levels of Ti in Au nanoparticles as in those of Figure 2G [11]. There are also bi-elemental material combinations in which one material, e.g. Pd due to specific chemical interactions, enhances plasmonic sensing on Au rods. An example of this is plasmonic detection of hydrogen-induced phase changes in 5-nm Pd nanocrystals in bimetallic Au-DNA-Pd hybrids (Figure 3A) [50]. In the last few years, methodologies to combine different materials into single particles and arrange plasmonic centres on the nanoscale has dramatically advanced due to improvements in particle synthesis techniques, like single particle manipulation, DNA-driven assemblies, and self-assembly that provide manifold opportunities in plasmonic sensing applications. “Nanoalloys” containing different metals in one particle are well known for their specific plasmonic properties that vary from that of the singular components [54]. Recently, however, control over stoichiometry and nanoscale positioning of multimetallic nanofeatures in polyelemental metal particles has been achieved [51]. Figure 3B shows the polyelemental metal nanoparticles obtained by scanning probe block copolymer lithography [51]. The technique can be used to combine several metals in extremely tailored composition, stoichiometry, and elemental positioning within single nanoparticles, which allows for tuning of plasmonic properties, hot spots, and reactive sites [51]. Furthermore, self-assembly techniques

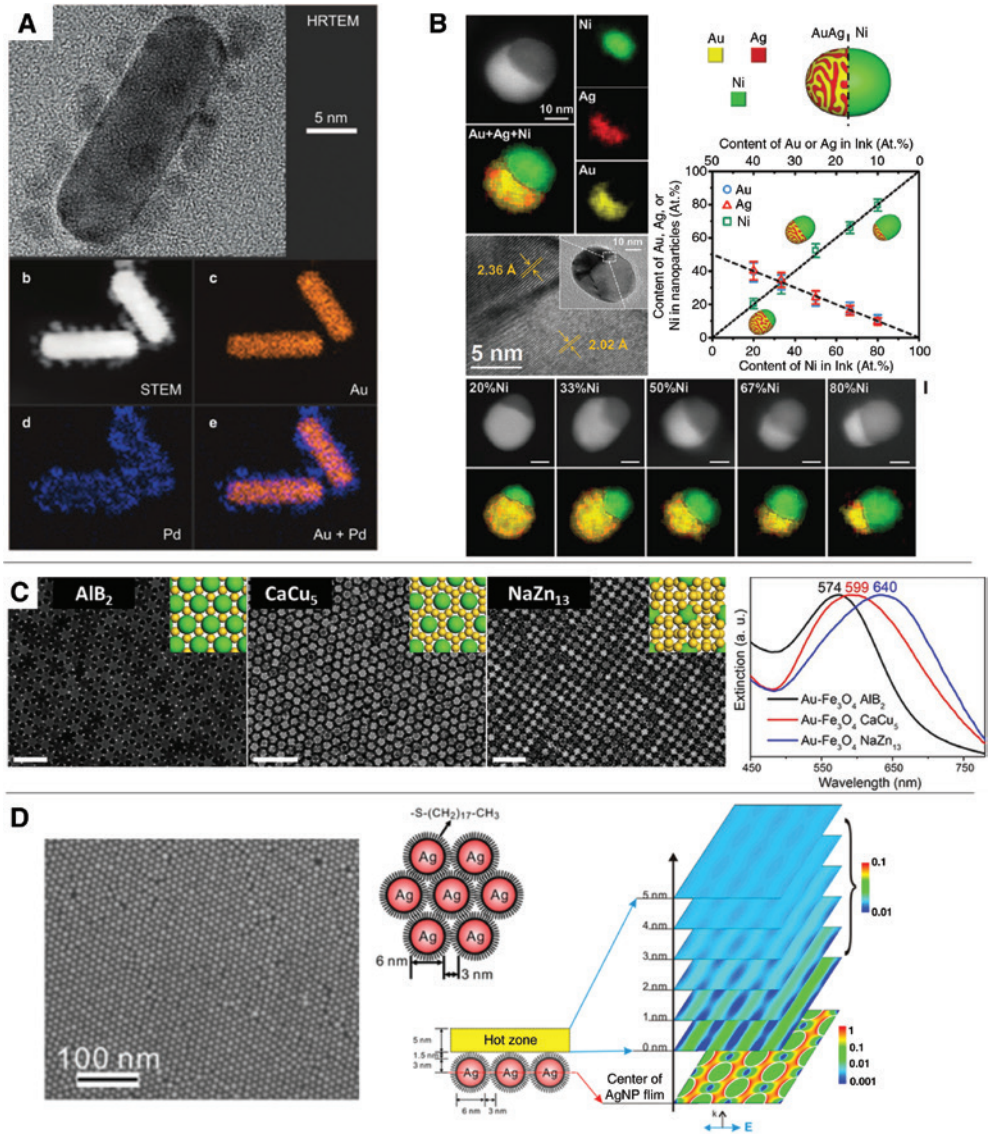

Figure 3: Functional combinations of plasmonic materials.
(A) High-resolution TEM image of sub-5-nm Pd nanoparticles after DNA-assisted assembly on a Au nanorod. The four panels below show scanning TEM (STEM) and element-resolved (energy-filtered) STEM images to represent the material distribution. This complex is used to sense hydrogen. Adapted from [50]. (B) Polyelemental AuAgNi heterostructured nanoparticles generated by scanning probe block copolymer lithography. There are different TEM micrographs, high-angle annular dark-field scanning TEM images, and energy-dispersive X-ray spectroscopy elemental mapping of AuAgNi nanoparticles with tailorable composition. The illustration shows a representative AuAgNi particle (24% Au, 24% Ag, and 52% Ni). Au and Ag are miscible and both elements are immiscible once Ni is added, resulting in a heterodimer. Adapted from [51]. (C) TEM images of binary superlattices assembled from 9.7-nm Au nanoparticles and 17.1-nm or 14.1-nm Fe_3O_4 nanoparticles. The crystallisation into AlB_2, $CaCu_5$, and $NaZn_{13}$-type superlattices determines particle spacing and plasmon coupling. The graph shows extinction spectra of superlattices on the left. Adapted from [52]. (D) Field-emission SEM image of a superlattice of 6-nm Ag nanoparticles used as a homogenous single-molecule SERS substrate. Illustrations of assembly, the SERS detection hot zone, and finite-difference time-domain simulated field patterns are present. Adapted from [53].

are used to position plasmonic particles into a hierarchical matrix of complex sensing regimes. DNA-driven assembly or self-assembly of monodisperse particles enables the control of nanoscale positioning and the distance between plasmonic nanoparticles and plasmonic hot spots [13, 42, 52, 53, 55]. Figure 3C shows an image of the co-assembly of monodisperse Au nanoparticles with Fe_3O_4 nanoparticles which grants controllable spacing and plasmonic coupling of the Au nanoparticles determined by the crystal structure of the resulting binary nanoparticle superlattice

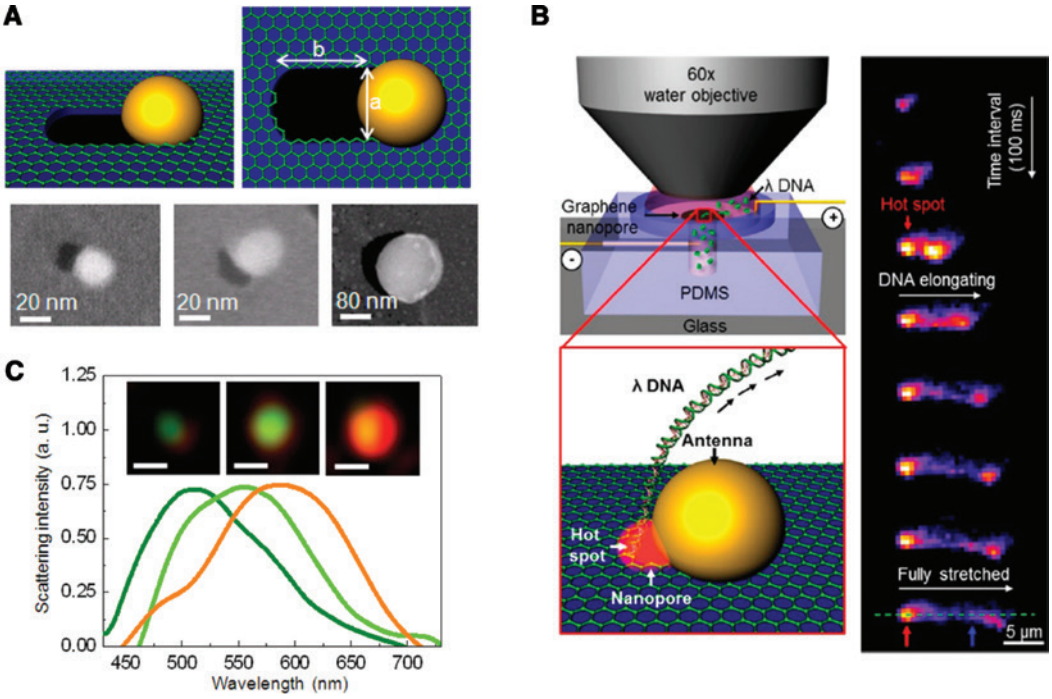

Figure 4: Graphene nanopore with a self-integrated optical antenna.
(A) Illustrations and SEM images of graphene nanopores and differently sized, integrated Au nanoparticles: 10 nm × 38 nm and 25 nm × 73 nm (short by long axis lengths) gold nanorods as well as 150-nm diameter gold nanospheres. (B) Darkfield scattering images and the corresponding spectra of plasmonic nanoparticles taken from nanopores with the self-integrated nanoantennae above, with a scale bar = 0.5 µm. (C) DNA translocation through integrated graphene nanopores with an optical antenna. The left inset depicts the device with its array of graphene nanopores and integrated nanoantennae. The right inset shows a zoomed-in view of plasmonically enhanced fluorescence of stained λ DNA when passing through the hot spot/opening. More specifically, it is a time series of confocal scanning fluorescence images of λ DNA translocation with a time interval of 100 ms. Adapted from [56].

[52]. Techniques to control distance and spacing of the hot spots are essential in large-area, quantitative SERS. The strong enhancement of single hot spots may lead to a false representation of the sample when the signal is mainly determined by a few detection sites [53]. Nanoparticle superlattices have shown the potential to counterbalance the inhomogeneous distribution of sensing hot spots and enhance the detection and performance of the sensor (Figure 3D) [53].

The combination of graphene with plasmonic metal nanoparticles is providing new and exciting opportunities. The plasmonic properties of Au nanoparticles can be used to tailor the integration of the particles into a graphene layer. Plasmon-driven photon-to-heat conversion enables the generation of a nanopore in a graphene layer with tuneable properties (Figure 4A and B) which can be exploited, e.g. for DNA sequencing [56]. The plasmonic Au nanoparticle at the graphene nanopore leads to a multifold fluorescent signal enhancement in detecting DNA elongation during translocation through the nanopore (Figure 4C) [56].

2.3 Surface chemistry and functionalisation

When plasmonic nanostructures and nanoparticles act as sensing elements in diverse applications, surface chemistry plays an important role. It is the active part of the sensor which mainly determines the type and specificity of the sensed surface interaction. Control over the surface chemistry of Au and Ag particles is provided by diverse reactions that exchange ligands, introducing functional groups, conjugate biomolecules like antibodies, proteins, and peptides, which always depend on the plasmonic material and its intrinsic surface composition (e.g. thiol ligands exchange citrate and cetrimonium bromide on Au) [12, 57]. Certain control over the local surface chemistry on single particles, e.g. the specific ligation of the tips of Au nanorods and nanostars, provides opportunities for specifical functionalisation of sensing hot spots [57]. Nevertheless, incomplete reactions, remaining ligands after functionalisation, unknown conformation, and the orientation of the conjugated molecules (e.g. when a specific binding epitope of a protein must be exposed and accessible for detecting

a binding reaction) still limit current and traditional SPR sensing approaches. To obtain the best possible signal, e.g. detecting biorecognition interactions, a pair of molecules is often used, e.g. an antibody and antigen or a receptor and ligand, whereby one of them is placed on the sensing nanostructure and the other is detected. If the molecule is placed on the plasmonic nanoparticle far enough from the sensing hot spot, the signal might be unfavourably low, and thus precise placement is necessary. Nanometer-precise single-molecule dropping techniques like an atomic force microscope (AFM) cantilever-based positioning method shown in Figure 5A may provide a way to exactly situate the molecules in the hot spots and thereby refine sensing capabilities and mechanisms [58].

Controlled surface chemistry for the active part of a sensor can create remarkable properties, such as it serving as an internal standard in SERS or creating defined spacing between numerous plasmonic particles or a substrate and particle [51, 58, 60]. Figure 5B shows tunnel junctions in Ag nanocube dimers obtained by defined particle spacing from surface functionalisations. The tunnel barrier width and height are controlled by the properties of the surface molecules [59]. Using electron energy loss spectroscopy, the tunneling charge transfer plasmon was observed with a frequency (ranging from 140 to 245 THz) dependent on the molecules bridging the gaps (Figure 5C) [59]. This direct experimental access to the tunneling charge transfer plasmon is extremely promising for novel single-molecule sensing [59].

2.4 Integrated systems and arrays

Integrating an array of plasmonic structures into a set of individual sensing regions provides the opportunity to perform analyses in parallel and to investigate complex compounds. Acimovic et al. presented a LSPR sensing chip based on Au nanorods that enables parallel, real-time inspection of 32 sensing sites distributed across eight independent microfluidic channels with very high reproducibility (Figure 6A) [61]. The array was used to detect cancer biomarkers down to concentrations of 500 pg/mL in complex biological environments like 50% human serum, which are realistic circumstances competitive with the standard yet laborious enzyme-linked immunoassays [61]. Light sources like plasmonic waveguide integrated

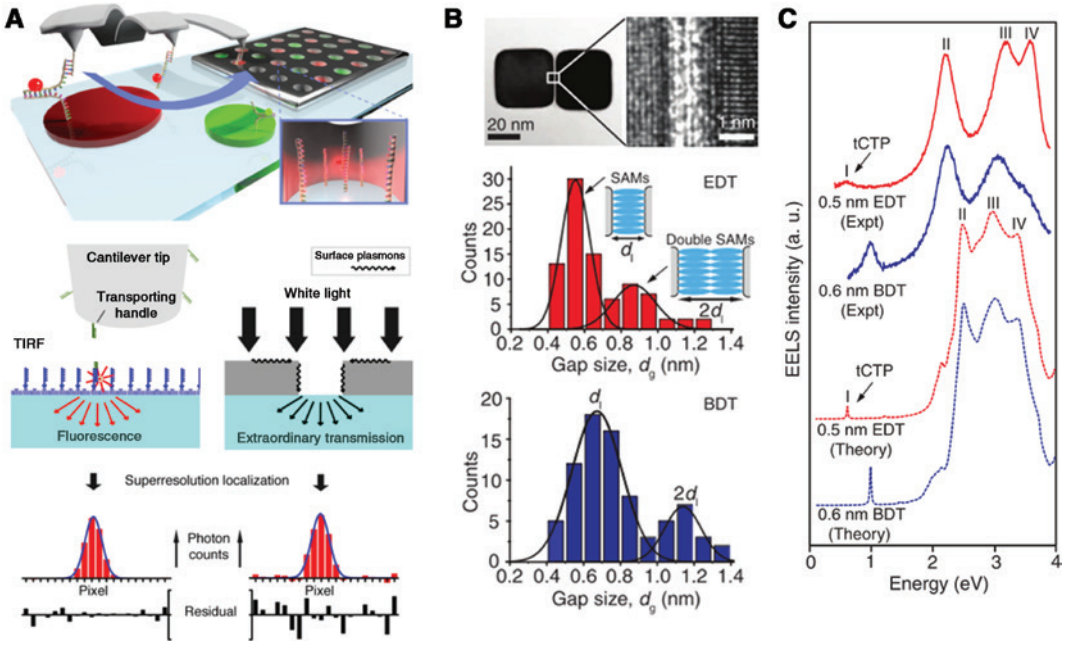

Figure 5: Surface functionalisation of plasmonic particles and hot spots.
(A) Functionalisation of plasmonic hot spots with single DNA molecules by an AFM cantilever. The position of the AFM's transporting handle is localised by fitting Gaussians to the fluorescence of a pasted anchor in total internal reflection fluorescence microscopy mode. Similarly, white light extraordinarily transmitted through the nanoaperture by surface plasmons is used to localise the apertures by Gaussian fitting of the intensity distribution. Adapted from [58]. (B) Direct observation of quantum tunneling between two Ag nanocubes bridged by tuning the surface molecules, with a high-resolution TEM image of the junctions and histograms of the gap sizes. Adapted from [59]. (C) Electron energy loss spectra with occurrences of quantum tunneling that are directly observable by tunneling charge transfer plasmon peaks. Quantum-corrected simulations of the extinction spectra confirm these peaks. Adapted from [59].

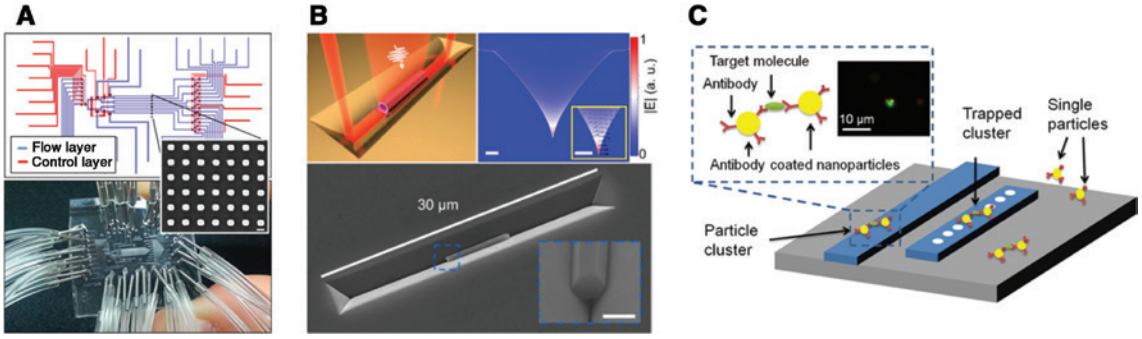

Figure 6: Arrayed and integrated plasmonic nanostructures.
(A) Schematic of the flow and control layers (upper inset) in a microfluidic chip (lower inset) that permit parallel LSPR sensing on 32 sensing spots consisting of arrayed nanorods. The inset shows a SEM image of the plasmonic gold sensors, with a scale bar of 200 nm. Adapted from [61]. (B) Hybrid nanowire gold V-groove plasmonic waveguide platform for an on-chip nanolaser source. The upper left panel is a representative illustration and the upper right panel is the electric field amplitude profile of the fundamental channel plasmon polariton mode supported by the V-groove waveguide at 870 nm. The scale bars here are 300 nm. The SEM angled view image below is of a GaAs/AlGaAs/GaAs nanowire positioned inside a 30-μm long V-groove, with a scale bar of 550 nm. Adapted from [62]. (C) Schematic of particle sensing with optical forces to trap and align the particles on waveguide-coupled silicon microcavities. Inset: Fluorescence microscopy image of a cluster with two polystyrene particles bound by green fluorescent protein. Adapted from [63].

nanowire lasers (Figure 6B) could eventually help miniaturise the detection platform towards the state necessary for sensing plasmon resonances directly on a chip [62].

For some applications, fixing plasmonic nanoparticles and structures to the functionalised device surface could be considered disadvantageous, e.g. as they are seldom reusable, given their surface functionalisation is preselected before use, and they are generally limited by the diffusion of the analyte molecules to the plasmonic particles [63]. Optical forces for trapping nanoparticles (like the aforementioned nanoholes for single-particle SERS [47]), open-access microcavities [64], or waveguide-coupled silicon microcavities as shown in Figure 6C [63] may be additionally considered for integrated sensors. In the latter example, a second probe laser detects the trapped particles (that were previously and separately exposed to the sample) by measuring the microcavity resonance shifts [63]. In open-access microcavities, the shift in cavity mode frequency during a trapping event provides information on both the nanoparticle and trap properties [64].

3 Whispering-gallery mode sensing: detection mechanisms, coupling, and time resolution

The field of optical microcavities has benefited tremendously from the use of ultrahigh-Q WGM modes excited in microspheres and microtoroids [65], lying at the frontier of ultrasensitive detection [66]. The perhaps most accessible WGM sensor is an approximately 100-μm diameter glass microbead. WGMs arise when light is confined for a prolonged time by total internal reflection inside the dielectric structure. High Q-factors have been observed when the light is guided inside a microsphere or other curved microstructures, such as wedge resonators [67], CaF_2 disks [68], a glass microsphere (with Qs as high as $(8 \pm 1) \times 10^9$) [69], a silicon ring [70, 71], or the toroidal glass microcavity [72]. Circumnavigation of the light results in optical modes that exhibit resonances with very narrow linewidths and that are useful for sensing molecules that interact with the evanescent field at the microcavity surface. The detection of molecules with a high-Q optical microcavity has the following primary merits: firstly, the light is recirculated in order to produce a large detection signal from multiple light-matter interactions with the molecule, and secondly, the confined light interferes with itself to form optical resonances at specific resonant wavelengths. Detection of physical, chemical, and biological entities is accomplished by tracking changes in the resonance frequency or corresponding wavelength with substantial accuracy. Resonant wavelength shifts of less than 1/100 of the linewidth of the optical resonance are typically resolved with WGM sensors [66]. In WGM biosensing, this sensing principle is called the "reactive sensing principle" as the sensor responds to the real part of the polarisability of biomolecules, viruses, or nanoparticles [1, 2, 4]. Another sensing principle relies on tracking changes in resonance linewidth. In this case, the sensor responds to the losses induced by a nanoparticle due to absorption

and scattering. Plasmonic nanoparticles [3, 73], dielectric nanoparticles [74], and virus particles [75] were detected in this way. A third sensing principle is the monitoring of split resonances by tracking the wavelength and linewidth difference of the split modes. This enables the sizing of bound, individual nanoparticles by tracking the mode splitting in high-Q microcavities [76]. The size of a dielectric particle such as a virus can be determined if the refractive index of the particle is known [76–79]. Particle-induced mode splitting has also been explored in WGM microlasers. Here, nanoparticles are detected by tracking the beat note that originates from the splitting of a lasing mode: 15-nm radius polystyrene nanoparticles, 10-nm gold nanoparticles, influenza A virions in air, and 30-nm polystyrene nanoparticles in water have been detected in this way [80]. Note that particle sizing was not possible with microlasers as the linewidth difference of the split modes was not measured. Single nanoparticle detection has even been demonstrated using split mode microcavity Raman lasers [81, 82]. A detection limit of 15 nm for a NaCl nanoparticle radius was achieved.

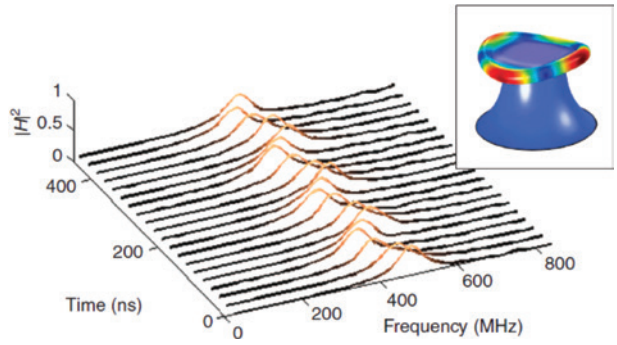

Figure 7: Cavity ring-up spectroscopy for ultrafast sensing with optical microresonators.
The probing laser is detuned from the WGM optical resonance at a fixed wavelength. The cavity ring-up sensing signal is generated by repeatedly switching the laser on and off. The ring-up signal can be acquired at a time resolution that is limited by the Q-factor: $t_{min} = Q/\omega_{Res}$. Adapted from [85].

Excitation of a WGM typically requires a coupler, such as a tapered fibre or prism. Recent works have explored the alternative of exciting WGMs in deformed microcavities using a free-space beam. Stand-off biodetection with free-space coupled asymmetric microsphere cavities was demonstrated [83]. Efficient free-space coupling was reported, with coupling of up to 30% of the incident light [84].

WGM sensors usually operate with time resolutions limited not by the sensor system itself but by the method employed to read out the resonator's spectral response. In swept-wavelength scanning, the time resolution is

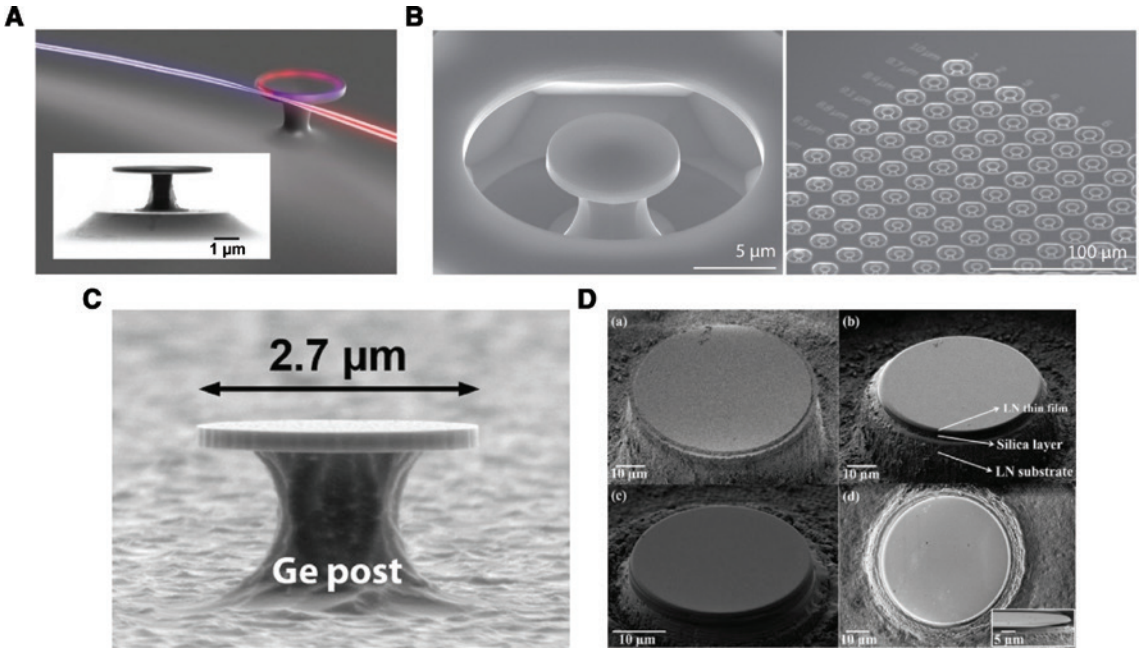

Figure 8: Materials for optical microdisk resonators.
(A) SEM image of a GaAs microdisk and depiction of the fibre-taper-coupling-based second-harmonic generation. Reprinted from [86]. (B) SEM images of a single monolithic diamond microdisk and an array of such structures. Adapted from [87]. (C) SEM micrograph of a pseudomorphic $Ge/Ge_{0.92}Sn_{0.08}/Ge$ quantum-well microdisk with a Ge post. Adapted from [88]. (D) SEM micrographs for lithium niobate microresonators, showing post formation via femtosecond laser ablation, two differently sized posts after focused ion beam milling, and the final product post-chemical etching and annealing, respectively. Reprinted from [89].

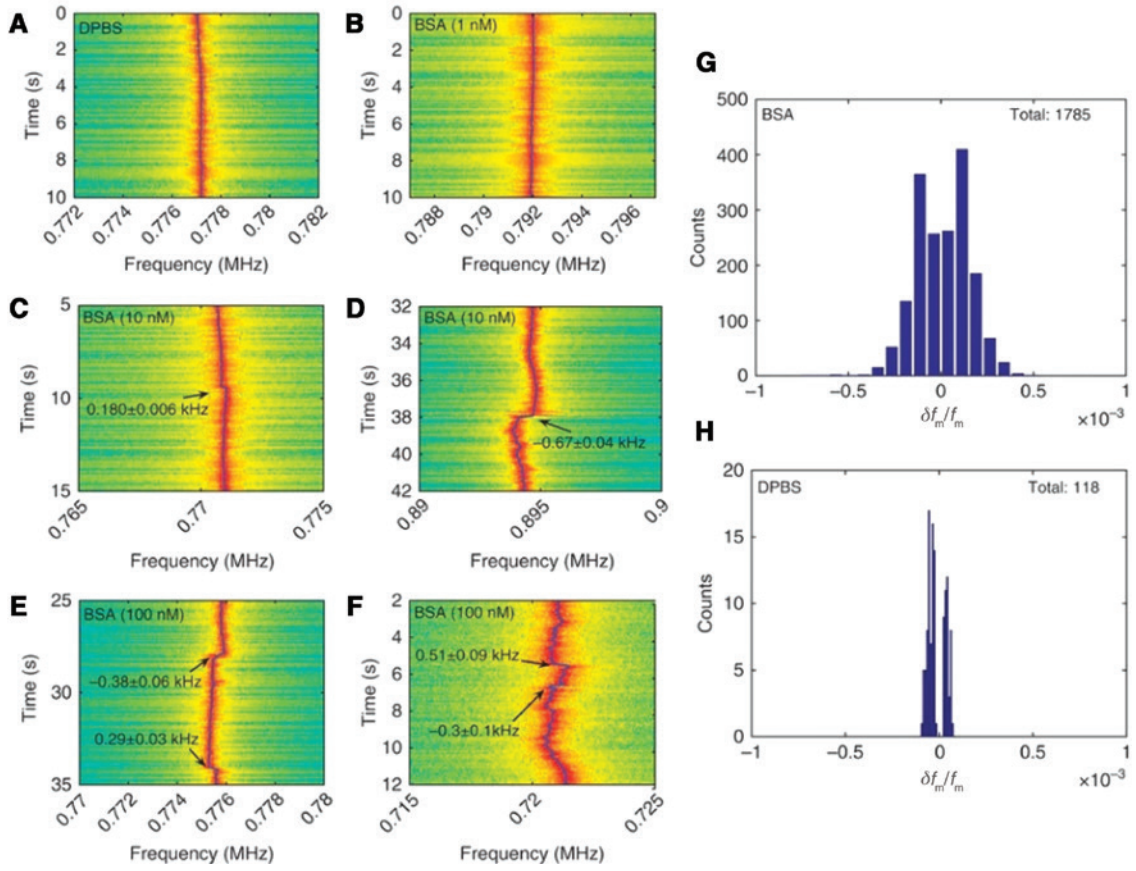

Figure 9: Sample mechanical spectrograms for a third harmonic tone and different BSA protein concentrations.
(A) Expected spectrogram for Dulbecco's phosphate-buffered saline (DPBS) as the external dielectric, without BSA. (B) Spectrogram for 1 nM of injected BSA, without binding events. (C) and (D) Spectrograms for 10 nM of injected BSA, with 180 ± 6 Hz binding and −670 ± 40 Hz release events, respectively. (E) and (F) Spectrograms for 100 nM of injected BSA, with several binding events wherein some exhibit frequency and background noise increasing over time. (G) and (H) Respective histograms of normalised frequency steps for BSA binding and the bare DPBS control. Reprinted from [96].

limited by the speed at which the laser wavelength can be scanned. In experiments by Rosenblum et al. [85] the time resolution is no longer limited by the tuneable laser system. Instead, a *Q*-factor limited time resolution was achieved by cavity ring-up spectroscopy (CRUS). In CRUS, the probe laser is detuned from resonance and switched on and off to create a broader spectrum around the laser's centre frequency, wherein parts of the laser spectrum are coupled into the microcavity. The WGM's lineshape and position can be obtained via Fourier transformation. The authors demonstrate CRUS for the detection of optomechanical motions with a nanosecond time resolution (see Figure 7).

3.1 Potential materials

Selection of microcavity materials and geometries allows for change in light confinement, the investigation of nonlinearities, and/or the sensing of different physical quantities. For instance, Kuo et al. [86] have exploited the high nonlinear susceptibility of gallium arsenide to generate a WGM second-harmonic spectrum (Figure 8A), while Haigh et al. [90] have enhanced Brillouin scattering by tuning of a magneto-optical yttrium iron garnet spherical cavity system. Recent materials/complexes of choice include diamond (Figure 8B) [87], constrained germanium-tin alloy (Figure 8C) [88], crystalline lithium niobate (Figure 8D) [89], high-*Q* magnesium fluoride [91], or caesium lead halide perovskite-coated silica [92]. There are also magneto- and electrostrictive materials that suffer deformations from an applied field [93] and some isotropic crystalline platforms whose thermal characteristics enable nano-Kelvin thermometry, e.g. near $80\ \mathrm{nK}/\sqrt{\mathrm{Hz}}$ [94]. The most obvious tradeoff, in the context of sensing, is made between resonator linewidth, mode volume, and the extent of the evanescent field beyond the outermost cavity interface. It is generally favourable to balance these

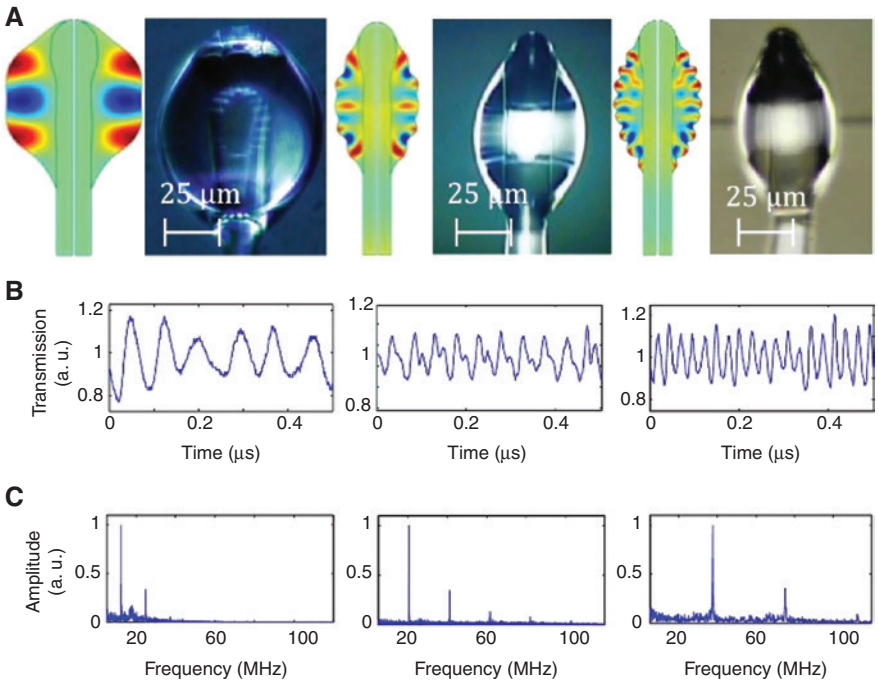

Figure 10: The optomechanics of droplets.
(A) Micrographs and acoustic mode patterns for droplets, with 99% of the energy found inside the liquid. (B) Time-domain oscillation measurements for the droplets. (C) Frequency-domain oscillation measurements for up to five visible harmonics. Droplet diameters are 40 ± 2 μm, 50 ± 2 μm, and 75 ± 2 μm, while predicted frequencies are 37.54 MHz, 20.57 MHz, and 12.45 MHz. Reprinted from [97].

parameters such that a maximal Q/V ratio is achieved. The sensing signal can thus be meaningfully increased by ensuring that the amplified electromagnetic field's overlap with the analyte is in a small region of interest.

3.2 Exploiting optomechanics

Circulating light that makes up a WGM can exert radiation pressure that actuates mechanical breathing modes. This foreground exists before a Brownian motion-driven background, as there are continuous displacements on the order of MHz that affect the microcavity resonance [95]. The radiation pressure-derived fluctuations can even overcome losses from fluid damping that would normally limit detection capabilities. With careful detuning towards higher frequencies in respect to the cavity resonance, it is possible to produce coherent oscillations with high finesse that, above a certain threshold, are regenerative. Their mechanical quality factor directly ties to an enhancement factor for the sensing resolution without a reduction in the detection region. In the same vein as WGM lineshape monitoring, the shifts in the mechanical resonance frequency can alternatively be extracted and analysed. A linewidth of 0.1 Hz centred at a frequency of 262 kHz, equating to a mechanical quality factor of 2.6×10^6, with higher-order harmonics, has been reported by Yu et al. and then employed as to detect proteins with masses of 66 kDa [96] (Figure 9). Such acoustic modes can be read out from cavities in liquid phase under ambient conditions as well [97] (Figure 10), opening the way for significant optomechanical interactions that lie between optical and mechanical degrees of freedom.

3.3 Nanoscale precision measurements and spectroscopy

As discussed previously, there are avenues for the measurement of weak forces in the presence of competing thermal Langevin noise. The motion of a mechanical oscillator can be seen as an incoherent radiation pressure force exerted by a nearby WGM. This has been quantified using energy averaging aided by gain from dissipative feedback, circumventing the scaling of the force resolution with the fourth root of the averaging time. Gavartin et al. found, in this particular case, that their lowest-power signal had a force spectral density of 15 $aN//\sqrt{Hz}$ while averaging over a ~35-s time window [98]. Nonlinear frequency conversion (i.e. cascaded four-wave mixing) underlying WGM-based Kerr frequency combs has also served to create precision frequency rulers in the mid-infrared regime [99].

Looking ahead to photonic-plasmonic hybridisation, dynamical backaction in cavities can be taken down to the level of molecular vibrations. SERS can be explored and enriched through observing the interplay between two parametrically coupled harmonic oscillators: a localised plasmon and molecular vibrational mode. By placing a plasmonic dimer at the cavity interface, one can effectively establish an anomalous Stokes/anti-Stokes intensity ratio, dependent on laser detuning [100] (Figure 11). Here, a narrow plasmonic resonance is desirable wherein light blue-detuned from it realises the vibrational pumping. The quantum mechanical origin of the scattering process was described by Schmidt et al. via bosonic operators under approximated energy landscapes [101].

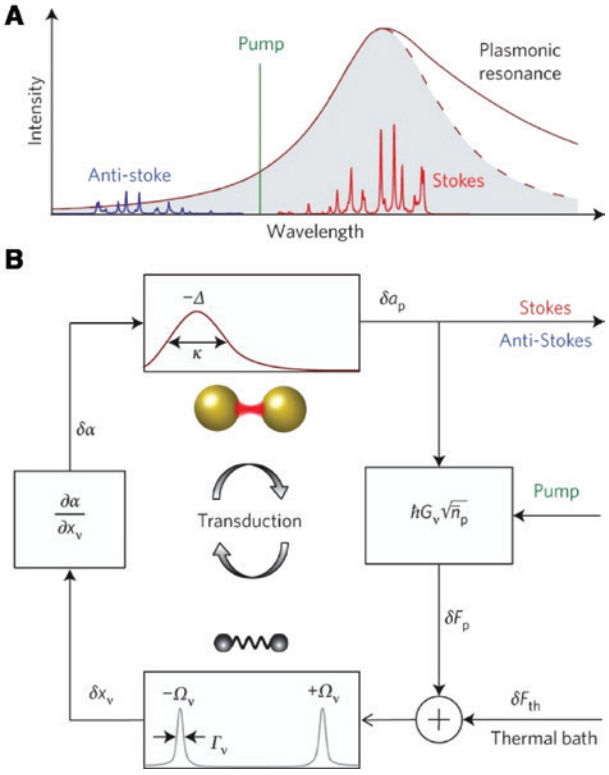

Figure 11: Dynamical backaction scheme for SERS. (A) Raman spectrum, with a pump (in green) that is positively detuned by roughly the vibrational mode frequency (Ω_v), a specifically enhanced Stokes signal (in red), anti-Stokes signal (in blue), and plasmon resonance (in brown). (B) Analogous feedback loop, with fluctuating variables about a mean (long arrows) and transfer functions (grey boxes). Starting at the pump, the power with a time-averaged plasmon occupancy of $\bar{n}_p$ controls the degree of amplification while transducing plasmonic field δa_p into force δF_p. Alongside the thermal force δF_{th}, δF_p is applied to the molecular displacement δx_v, and the plasmon-molecule oscillator filter has a linewidth Γ_v at $\pm\Omega_v$. The loop is then closed by transduction of the displacement into a polarisability change $\delta\alpha$ through Raman activity $\delta\alpha/\delta x_v$, considering that the localised plasmonic field is modulated. Reprinted from [100].

3.4 Optoplasmonic sensors: single-molecule detection

Combining photonic and plasmonic sensing techniques into optoplasmonic sensors drastically heightens detection signals as compared to the individual sensor structures they are composed of, enabling the detection of single biomolecules and ions. The physical mechanisms behind hybridisation of photon-plasmon modes and their influences are not completely understood, demanding theory that surpasses a first-order perturbation approach to resonance shifts from dielectric adsorption [102]. This has been expanded upon by adopting generalised Lorenz-Mie theory [103] and level repulsion [104], allowing for more accurate resonance shift predictions and an explanation for both redshifts and blueshifts when plasmonic nanoparticles encounter an optical WGM microcavity.

The possibility for improving detection sensitivity on a hybrid photonic-plasmonic system was realised only recently and first examined for microsphere WGM sensors coupled to plasmonic nanoparticles [105–108]. The specific detection of individual biomolecular interactions was demonstrated on a WGM microsphere/plasmonic nanorod sensor system (see Figure 12A, B, and D) [3]. The nanorod was modified with an oligonucleotide to demonstrate the detection of receptor-specific interaction kinetics with complementary oligonucleotides in solution, down to single 11-mer oligonucleotides. The interaction kinetics were found to be markedly different for strands that contained a single nucleotide mismatch [3]. In the same study, small molecules with less than 1 kDa molecular weight were detected individually as they intercalated in a double-stranded DNA oligonucleotide [3]. The single-molecule nature of detected events was verified statistically, by confirming an underlying Poissonian process and by confirming first-order reaction kinetics with an event rate that scaled linearly with concentration [3, 109]. This all-optical approach resolves transient as well as permanent interactions of single ligand molecules at the nanoparticle interface in situ (Figure 12F and G). Reaction kinetics can thus be monitored over a broad range of affinities and especially under conditions where no reaction product is formed on average. This enables the real-time observation and characterisation of reactions during the entire procedure of a bottom-up surface modification (Figure 13A and B), ranging from the deposition of ligands to the confirmation of their functionality [110]. The optoplasmonic single-molecule technique was used to investigate the reactions of amines and thiols with the surface gold atoms of a nanorod (Figure 13C and D). The reactions were monitored from low to high affinity by adjusting ionic strength and pH of the reaction buffer

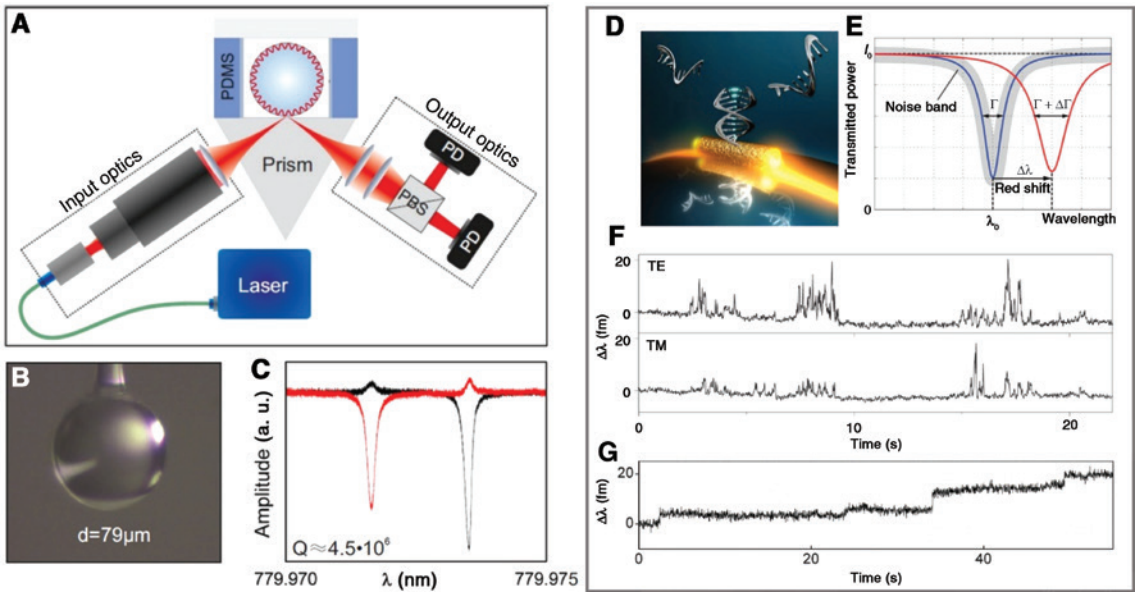

Figure 12: Detection of single DNA molecules and their interactions with optoplasmonic sensors.
(A) A prism is used to couple light into the WGM of a glass microsphere for monitoring single molecules on a gold nanorod. (B) The glass microsphere is approximately 80 μm in diameter and modified with a gold nanorod for highly sensitive detection. (C) WGM spectra acquired by swept-wavelength scanning of a tuneable laser source, operating at a wavelength of ~780 nm. (D) The nanorod attached to the microsphere sensor is modified with oligonucleotide receptors. (E) Binding of a DNA fragment from solution to an individual oligonucleotide receptor results in a resonant wavelength shift of the WGM. (F) The transient interactions between a DNA fragment and an oligonucleotide receptor appear as spikes in the wavelength shift signal, where each spike corresponds to a single-molecule interaction event. The interaction kinetics transition from the transient (F) to the permanent binding regime (G) dependent on the sequence of oligonucleotide receptors that is attached to the nanorod. Adapted from [3].

[110]. Transient interactions due to adsorption and desorption of the molecules could be readily discriminated from permanent interactions due to the formation of covalent bonds. It was also found that the thiol and amine groups occupied different binding sites (protruding and non-protruding gold atoms) on the nanorod. Additionally, the influence of different ligand molecules such as DNA oligonucleotides and polyethyleneglycols (PEG) on the reaction kinetics of their amine and thiol head groups with the gold atoms was investigated (Figure 13E). The real-time feedback of the hybrid sensor system enabled the rapid development of reaction conditions favourable for the covalent conjugation of ligands. In this way, single-stranded DNA and biotinylated PEG molecules were permanently immobilised at the sensor surface. The functionality of the immobilised receptor molecules was demonstrated by recording sensor signals due to the specific binding of complementary DNA strands and anti-biotin antibodies, respectively (Figure 13F). Investigations of inhibition of ligand surface reactions, i.e. of a thiol-DNA interaction in the presence of small amounts of sodium dodecyl sulfate (SDS) as seen in Figure 13G, were possible. This is usually unachievable via ensemble-based techniques as the amount of product in the reaction is extremely low in the presence of inhibiting SDS.

Beyond the ability to sense single molecules [74], hybrid WGM-plasmonic systems have resolved surface interactions involving single Zn^{2+} and Hg^{2+} ions attracted to binding sites on gold nanorod antennae [109] (Figure 14). Ion channels in biological organisms and catalytic reactions could be controllably probed as is made plausible by the repulsive zones formed by positively charged cetyltrimethylammonium bromide partially coating the nanorods. Three interaction regimes, set by the ionic strength and hence degree of Debye screening, exist with distinct temporal signatures (Figure 15). The assumption that ion detection is based on a Poisson process is confirmed by statistical analysis of event rates. Moreover, this observation, together with the linear dependence of the rate on the concentration, demonstrates that the observed spike events originate from only a single ion interaction. The nature of possible charge transfer mechanisms during the spike and step events in the time traces remains unclear; however, further studies with diverse electronic preconditions could clarify this. Further theoretical investigation into which property of the analyte ions is causing the shift and how it affects the localised surface plasmon excited in the nanorods could clarify the magnitude of the observed sensor signals and their frequency. Looking

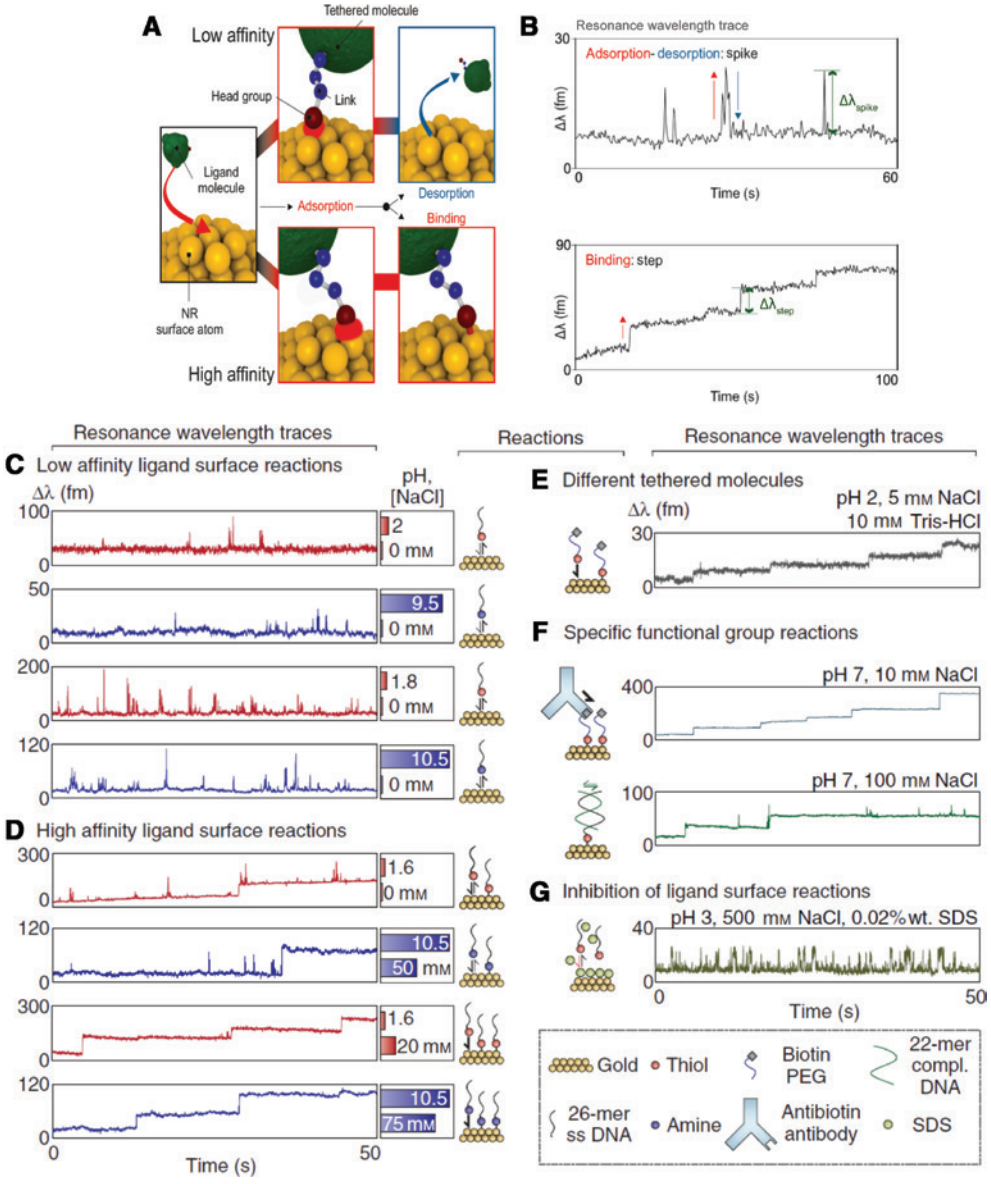

Figure 13: Probing single-molecule surface reactions with optoplasmonic sensors.
(A) Surface reactions with low and high affinity. (B) The corresponding single-molecule WGM sensor signals. Spikes indicate low-affinity reactions, while steps indicate high-affinity reactions. (C–G) Overview of reactions monitored with a hybrid photonic-plasmonic single-molecule sensor. Adapted from [110].

at the electronic configuration in zinc and mercury, they both possess d subshells. In terms of the actual excitation of propagating surface plasmon polaritons (SPPs), Min et al. [111] coated microdisks with a thin layer of silver that supported such modes and attained high Q/V ratios primarily limited by intrinsic metal losses.

The coupling regimes for periodic arrangements of identical plasmonic particles along the equator of a WGM have been treated theoretically [112], and single-particle absorption spectroscopy with hybrid WGM-plasmonic devices has been conducted experimentally [113] (Figure 16). For the latter, dense sets of Fano resonances could make modalities like coherent anti-Stokes Raman spectroscopy [114] within reach. Such functionality, combined with an *in vivo* implementation that extends to macroorganisms, constitutes a penultimate vision for optoplasmonic technologies in the field of biosensing.

Some experiments with optoplasmonic sensor systems have already demonstrated their capability of monitoring structual dynamics of single protein molecules. One of the first label-free optical methodologies for observing the conformational changes of an enzyme, e.g. single enzyme-reactant interactions, has appeared in the literature [115]. The motions/dynamics of the polymerase enzyme are

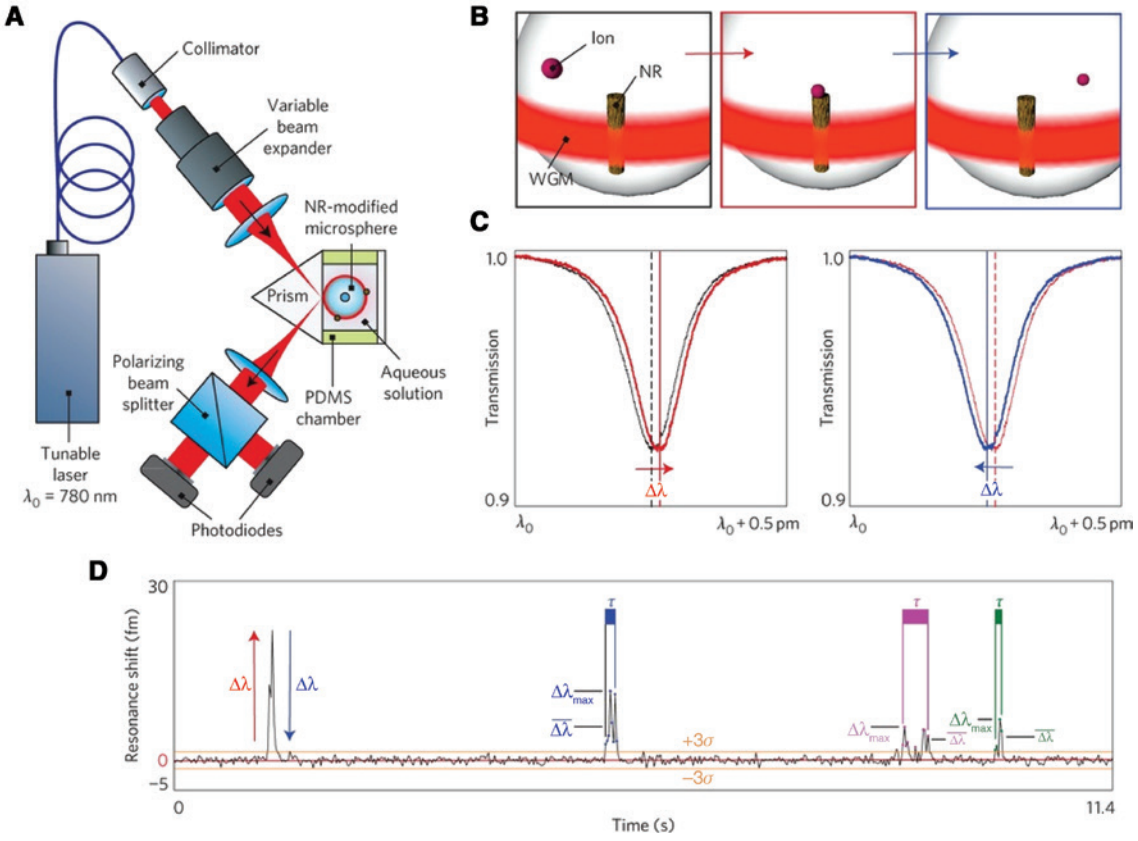

Figure 14: WGM sensing technique for single-ion detection.
(A) Experimental configuration for prism-based excitation and probing of optical WGMs. (B) and (C) Zinc and mercury ions transiently interacting with bound gold nanorods, generating a redshift when encountering and then a blueshift when leaving the hot spot. (D) Time trace of the resonant wavelength wherein there are discernable ion detection events. Reprinted from [109].

thereby construed as shifts in the WGM wavelength $\Delta\lambda_{Res}$. The WGM wavelength shift signal is proportional to the electric field intensity integrated over the volume of the biomolecule and the polarisability of the molecule in excess of the medium α_{Ex}. Consider, for example, the opening and closing of the polymerase enzyme as is shown in the inset of Figure 17. This motion of the polymerase causes a change in the volume of the molecule overlapping with the near field of the WGM sensor over time, thus translating to a resonance shift $\Delta\lambda_{Res}$. To reiterate, the data in [115] proves that the platform can investigate structural state transitions in single molecules without labels.

4 Photonic crystals engineered with nano/microcavities for integrated sensing

Each successive generation of biosensors based on nano/microoptical cavities demands not only optimised figure of merits, e.g. raised Q-factors and lowered mode volumes approaching physical limitations, but at the same time a compatibility with efficient integration/miniaturisation. This not only presents challenges for conventional optical biosensors yet also calls for a paradigm shift in the very design of optical biosensing devices. In this section of our review we outline the recent advances in one of the promising avenues for integrated biosensing: PhCs and their engineered variants that can effectively realise a lab-on-a-chip. Unlike well-established, integrated solid-state technology for the confinement of electrons in a medium that exploits naturally available periodic crystals with electronic bands, it is far more difficult to confine light in a very small spatial volume with long and efficient light-matter interactions given the materials available [116]. A natural step in this direction would be artificial nanostructuring of a homogenous medium and moulding it into an improved "photonic interaction-conducive periodic crystal" with photonic band properties. The rationale behind this was to facilitate an enhanced interaction between photons and the material medium in a

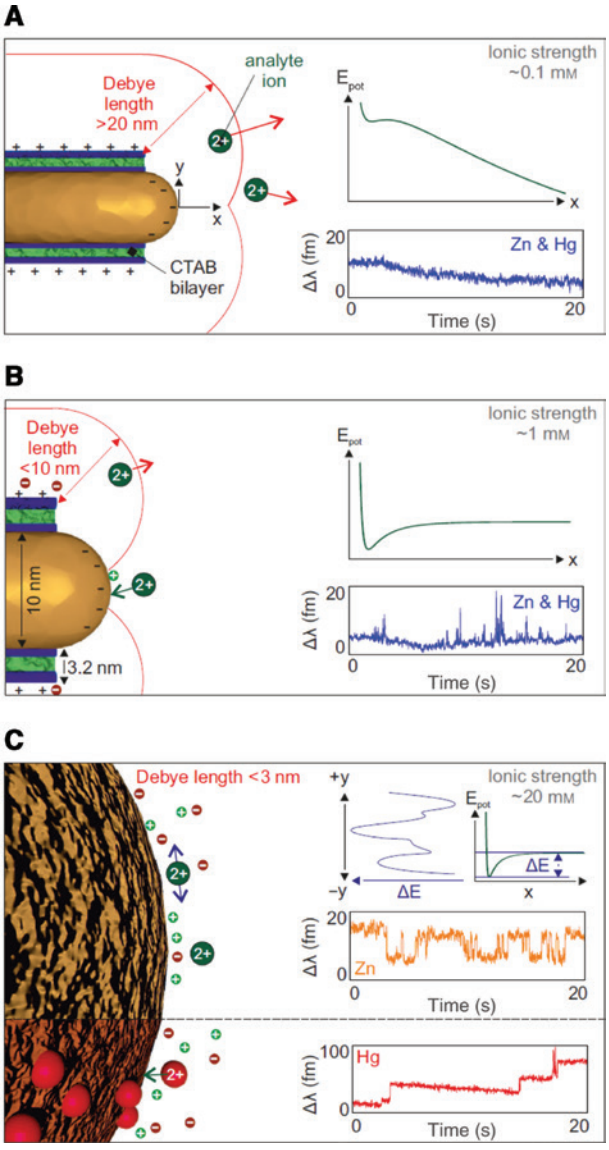

Figure 15: Optical observation of single atomic ions Zn^{2+} and Hg^{2+} interacting with plasmonic nanorods in solution.
The detection signal has been boosted with optical microcavities. Three different interaction regimes were observed: (A) complete screening of ion-nanorod interactions with no spikes or steps at low ionic strengths, (B) restriction of the attractive region with temporally short interactions at roughly 1 mM ionic strength, and (C) Zn analyte ions confined for longer periods of time in the local minimum and Hg permanently bound at high ionic strengths. Reprinted from [109].

controlled manner, like electrons in a solid-state crystal. Though the concept of periodic medium-enabled light matter interactions historically dates back further than a century [117], active research in the field of PhCs was triggered a few decades ago with seminal works by Bykov [118], Ohtaka [119], Yablonovitch [120], and John [121]. A PhC is a material with periodic modulation of its refractive index where, for practical applications, the periodicity is expected to be comparable to the desired wavelength of light in the material. Depending on the complexity of desired degrees of freedom on control of light propagation, this periodic refractive index modulation could be realised in one dimension (1D, i.e. Bragg mirrors), in two dimensions (2D), or in three dimensions (3D) [122].

In principle, similar to their solid-state counterparts possessing an electronic band gap, these materials can be designed and fabricated with a photonic band gap (PBG). This prohibits light propagation within a desirable range of frequencies, while the rest of the light wave propagation is dictated by the dispersion relation of the photonic bands. A rigorous overview of the different aspects of PhCs can be found elsewhere, with their peculiar light-matter interaction behaviour (e.g. negative refraction, superprism effect, etc.) pertaining to diverse applications ranging from simple optical filters/couplers to futuristic optical cloaking [122].

Considering the complexity involved in fabricating real 3D PBG materials for practical integration, 1D PhC surfaces and strongly modulated 2D PhC slabs of submicron thickness have been widely investigated for integrated nanophotonics applications, even for sensing at the point of care [123–127]. Like basic PBG principles, the photonic band properties in these 2D nanoengineered materials originate from multiple instances of beam scattering and interference at the photonic lattice due to periodic perturbation of the structure. PhCs respond very differently to the incident light in comparison to the response of an unstructured homogenous material slab as shown in Figure 18A and D [116, 128]. The 2D PhC crystal slabs have PBG-dominated beam guidance along the plane of the slab defined by the electric field polarisation of the incident beam, whereas there is total internal reflection-dominated index guidance perpendicular to the plane of the slab.

The spectral dispersion of these PBG engineered materials has very distinct control on light confinement and slow light properties within them where the group velocity, $v_g = d\omega/dk$, is drastically altered especially near the band edges [128, 129]. This in turn results in long and very efficient light-matter interactions which would otherwise be improbable in a homogenous medium. Further enhancement and precise control by optimised defect engineering in a PhC gives rise to a guided mode within the PBG [116], similar to dopant trap energy levels in an extrinsic solid-state crystal. This extreme light confinement in localised modes, down to very small volumes, makes them attractive candidates for integrated biosensing applications. These engineered nano/microcavities engraved within microchip-sized PhC biosensors have larger Q-factors

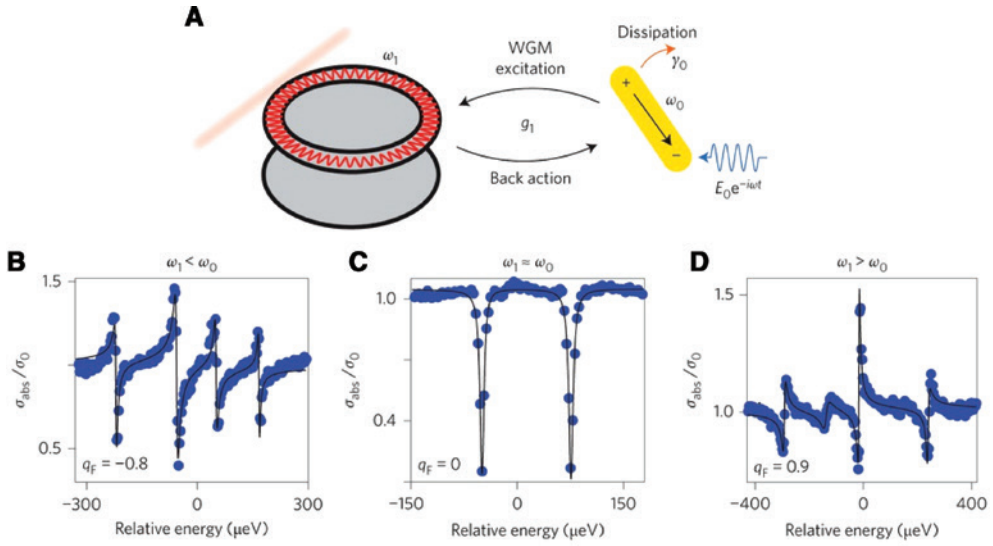

Figure 16: Pictorial description of coherent interactions between WGMs and localised surface plasmons.
(A) There is pumping of the localised surface plasmon via a time-varying field $E_0e^{-i\omega t}$ with dissipation of energy at a rate of γ_0. The overlap between the WGM and localised surface plasmon is characterised by g_1, while their respective resonance frequencies are ω_1 and ω_0. (B) Fano resonance (black line) and experimental spectrum (blue dots) for $\omega_1 < \omega_0$, with destructive interference at higher energies and constructive interference at lower energies. (C) Fano resonance and experimental spectrum for $\omega_1 \approx \omega_0$, with destructive interference only. (D) Fano resonance and experimental spectrum for $\omega_1 > \omega_0$, with destructive interference at lower energies and constructive interference at higher energies. Reprinted from [113].

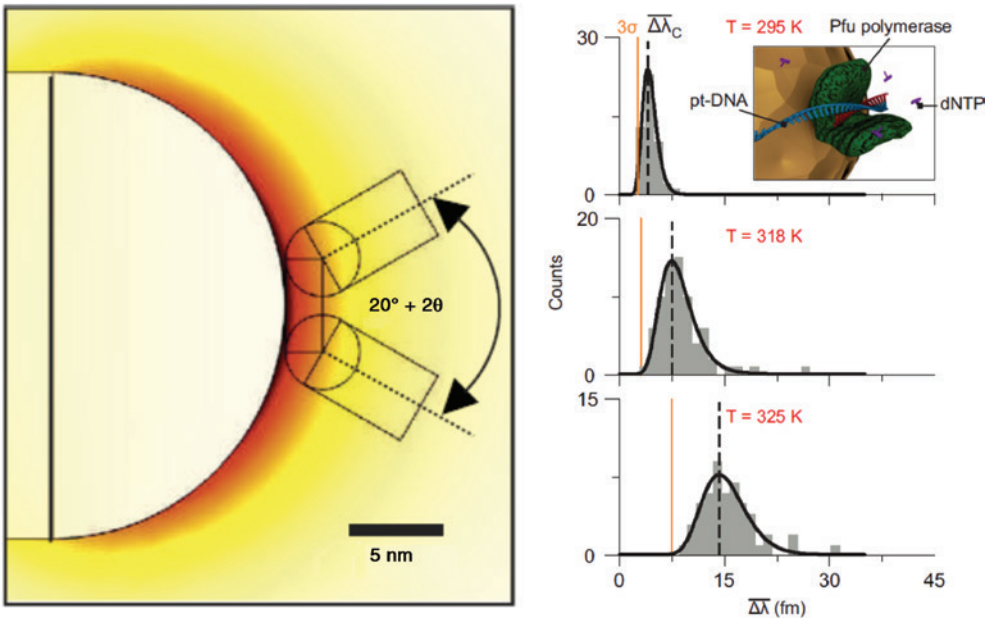

Figure 17: Histograms of the WGM wavelength shift for the opening and closing of the polymerase enzyme "hand".
The motion of the polymerase causes a change in the volume of the molecule overlapping with the near field of the WGM sensor, producing WGM shift signals with increasing amplitude as the temperature increases. Furthermore, this is elucidated by the motion of the polymerase which increases with the increase in the enzymatic activity associated with DNA synthesis (here, it is Pfu polymerase). Adapted from [115].

proportional to longer photon lifetimes, augmenting interactions with the analyte for label-free detection. As the present review focuses on recent advances in optical microcavities for chemical and biomolecular sensing, we will mostly direct our discussion towards biosensors based on engineered nano/microcavities in PhCs.

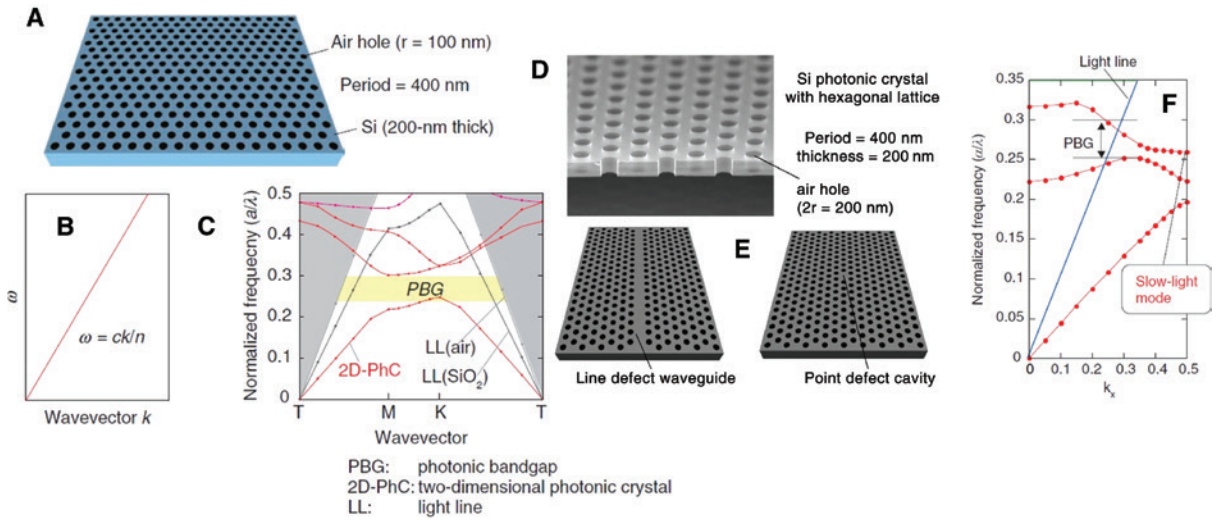

Figure 18: Photonic crystal structures and their optical properties.
(A) Schematic diagram of a 2D hexagonal PhC slab with etched air holes fabricated from a SOI wafer. (B) and (C) Light dispersion in conventional materials and in the given silicon PhC, respectively. Adapted from [128]. (D) SEM micrograph of a 2D Si PhC slab. (E) Engineered defects in a 2D PhC slab W1 line-defect waveguide (left) and point-defect cavity (right). Adapted from [116]. (F) Light dispersion in a line-defect waveguide in a similar silicon hexagonal air-hole PhC. Adapted from [128].

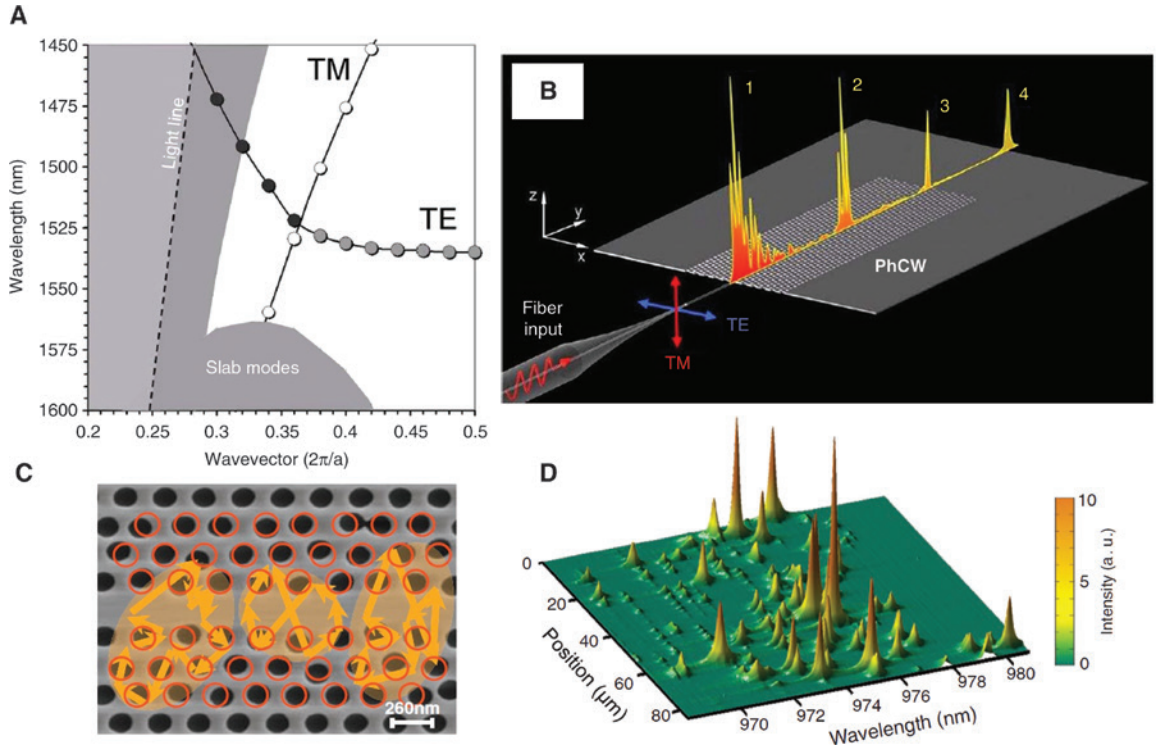

Figure 19: Disordered PhC structures that exhibit Anderson localisation of light.
(A) Photonic band structure around the quasi-transverse electric (TE) mode edge showing both quasi-TE and quasi-transverse magnetic (TM) guided modes for a hexagonal PhC with air holes etched in the oxide layer of an SOI chip. (B) Excitation of high-*Q* random cavities in a tapered fibre-coupled W1 waveguide engineered in a PhC slab. Marked features in the surface emission (i.e. orange peaks) represent the scattered light intensity from Anderson-localised random cavities at (1) the input facet, (2) inside the waveguide, (3) at the waveguide output, and (4) at the cleaved facet. The TE and TM polarisation of the excitation beam are denoted by the blue and red arrow marks. Adapted from [130]. (C) PhC waveguide with 6% engineered disorder, wherein the holes in the ideal PhC structure without engineered disorder are shown as red circles and the wave vectors of localised modes point along the orange arrows. (D) Photoluminescence spectra collected from a 3% disordered sample at 10 K. The excitation and collection microscope objectives were scanned along the waveguide. Adapted from [132].

Both engineered point defects and line defects (Figure 18E) in slab PhCs with air holes and their performance optimisation through structural modification of lattice basis structure surrounding the engineered defects will be reviewed. PhC-based nano/microcavities are particularly interesting for integrated biosensing, including PhC slotted waveguides, nanobeam cavities, and PhC nanoslotted laser arrays. We end this section by detailing very recent developments in hybrid plasmonic-photonic PhCs for biodetection, even reaching the single-molecule level, as to illustrate their suitability for integrated biosensor design.

As was previously mentioned, the light confinement in the engineered point or line defects (i.e. waveguides) in the PhCs grants a long light-matter interaction time. The large effective group velocity near the band edge for the guided modes within the band gap (see Figure 18C) hints to their intrinsic characteristics to be utilised for biosensing. One of the very interesting features within these PhC waveguides is the residual or intentional disorder which creates high-Q Anderson-localised nanocavities [130, 131]. As is shown in Figure 19A and B, the spectrally sharp resonances centred around the cutoff wavelength are from interference of coherently scattered electromagnetic waves that forms narrow localised bands with spectrally distinct quasistates [130]. This effect could be further enhanced by adding a single layer of quantum dots in an intentionally disorder-engineered PhC waveguide as is shown in Figure 19C and D [132, 133]. These disorder-assisted coupled random cavities in PhC waveguides are promising for advanced biosensing.

Strong light confinement in integrated nano/microcavities implies that photons remain in a restricted physical space for extended periods of time [116]. One very efficient means to achieve this confinement is through heterostructured PhC waveguides engineered with width-modulated nanocavities where the holes near the waveguide are slightly shifted (i.e. by a few nanometres) in a well-controlled manner [133], as can be seen in Figure 20. In principle, this does not change the original loss-free mode profile [133]. In Figure 20D and E, numerical results in such cavities (with higher quality factors and smaller mode volumes) are given. In a recent experimental realisation of air-bridge-type heterostructure nanocavities fabricated from silicon-on-insulator (SOI) substrates within well-controlled environmental conditions, a Q-factor above 11 million was reported with the longest observed photon lifetime of 9.2 ns [134]. These findings set the bar for precisely engineered nanocavities in PhCs for the next wave of exotic biosensing applications.

Now that we have given a glimpse of the background and a few select developments pertaining to

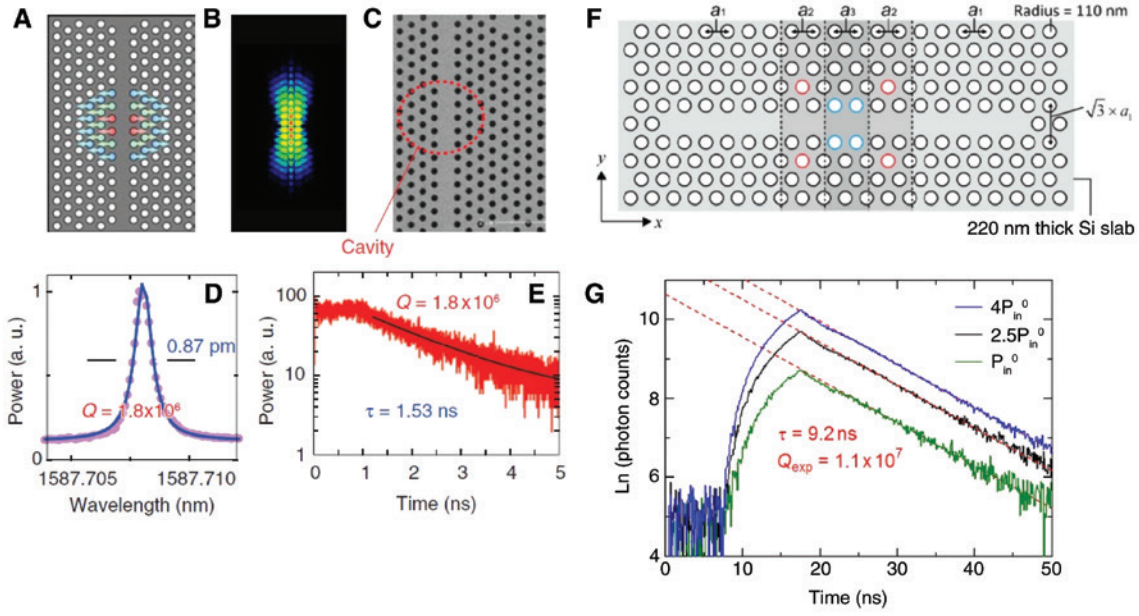

Figure 20: Photonic crystal structures designed to include high-Q nanocavities.
(A) Ultrahigh-Q PhC nanocavities. (B) The associated computational design of a width-modulated line-defect cavity in a Si hexagonal air-hole PhC (i.e. calculated field intensity profile). (C) SEM image of the actual fabricated sample. (D) Experimentally recorded transmission spectrum and (E) time-resolved measurement of the output intensity decay from the cavity. Adapted from [128]. (F) and (G) Heterostructure nanocavity resulting in experimental Q-factors greater than 1.1×10^7. The designed heterostructure PhC nanocavity is featured above, while the photon decay curve is below. Adapted from [134].

nano/microcavities in PhCs, we will proceed to discuss advanced architectures and/or methodologies based on PhC nanocavity-assisted label-free biosensing. For the past couple of decades there has been intense research in the field of biochemical detection [126, 127, 135]. Here, we will mainly restrict ourselves to the past decade and cover very recent milestones. The wavelength shift corresponding to the refractive index change in the sensing area of PhC nano/microcavities can be due to the binding of various biomolecular analytes, such as bovine serum

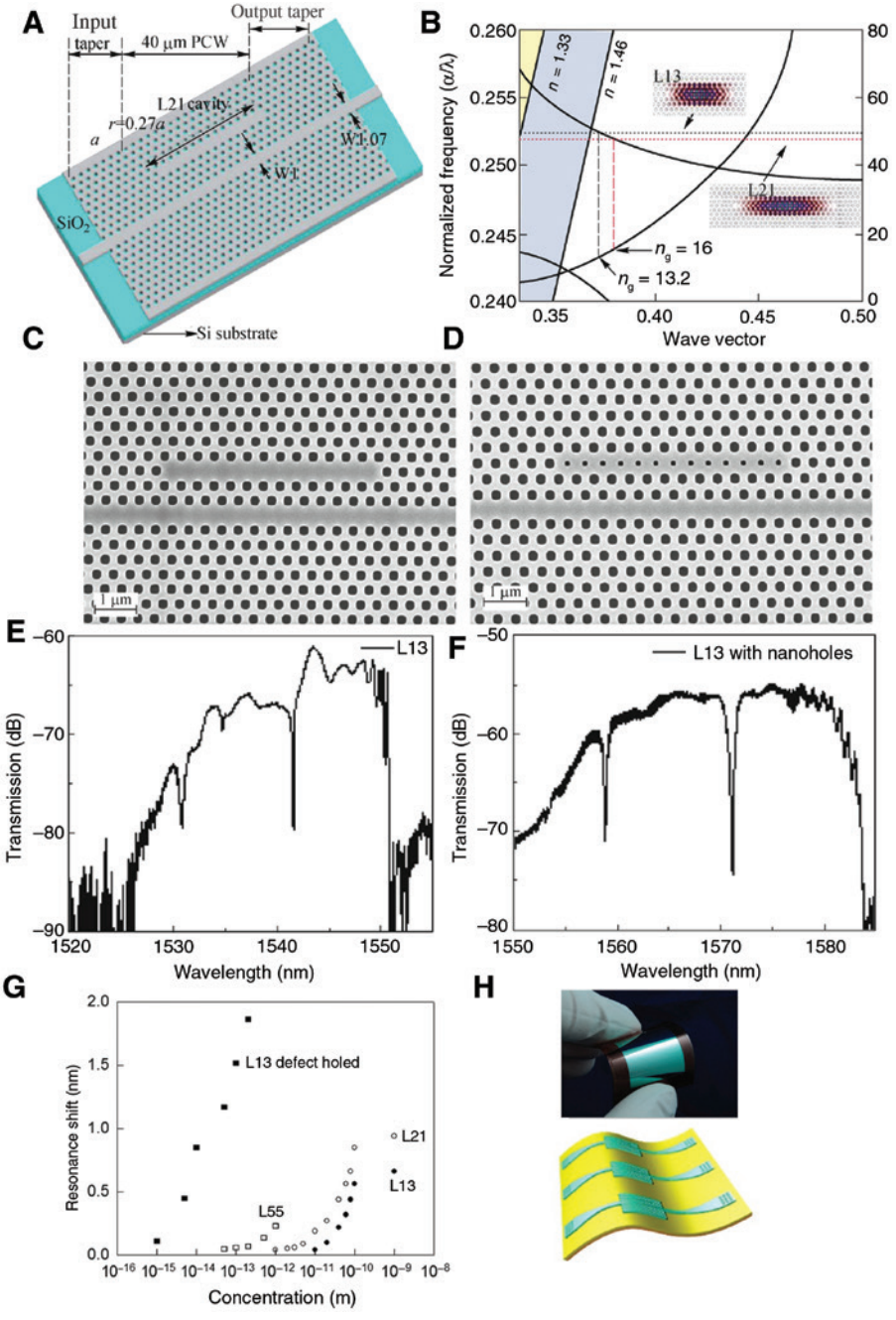

Figure 21: Photonic crystal defect cavity based sensors.
(A) Schematic of one of the PhC microcavity devices for biosensing. (B) Dispersion diagram of a W1 PhC waveguide in water. The black and red dashed lines indicate the frequencies of resonant modes for L13 and L21 PhC microcavities. The mode profiles are given as insets. Adapted from [183]. (C)–(F) SEM images of a L13 PhC microcavity with and without nanoholes. Their transmission spectra with a number of sharp resonances are found below them. Adapted from [183] and [184]. (G) Biosensing spectral shifts in L21, L55, L13, and L13 defect holed PhC microcavities. Adapted from [185]. (H) Flexible silicon nanomembrane PhC microcavity (i.e. 2 cm × 2 cm nanomembrane) on polyimide film and a schematic of the film peeled off from the mechanical support. Adapted from [186].

albumin (BSA) proteins [136–143], single-stranded DNA [144], optically trapped bacteria [145, 146], NCI-H358 lung cancer cell line lysates [147], and human papillomavirus virus-like particles [148–150]. Sophisticated slotted waveguides [141, 151–153] as well as nanobeam cavities [140, 146, 150, 154–160] have also been implemented for analyte-specific stoichiometric studies and biomolecule micromanipulation. Extreme, sub-attomolar detection of a streptavidin protein was reported for nanoslot PhC nanolasers [139, 161–168], while novel PhC nanocavities combined with plasmonic nanostructures have emerged as hybrid photonic-plasmonic biosensors [169–179]. Unusually sensitive biodetection down to the single-molecule level with nanostructured materials comprising self-assembled silver nanoparticles on PhC diatom biosilica [180, 181] and a gold antenna-in-a-nanocavity [182] substantiates the fast and steady advancement of hybrid photonic-plasmonic instrumentation utilising PhCs.

An analysis of one exceedingly efficient PhC microcavity geared for biosensing applications is given in Figure 21 [183–186]. The schematic (Figure 21A) displays a linear PhC microcavity denoted as Ln, where n is the number of missing holes, designed two periods away from the PhC waveguide (W1). In Figure 21A, n = 21, and in Figure 21B, the dispersion diagram is for L13 as well as L21 PhC microcavities. A variant of the linear PhC microcavity with and without etched holes within the defect region is shown in Figure 21C–F for the detection of plasma proteins in samples with pancreatic cancer. The fabrication feasibility of flexible single-crystal silicon nanomembrane PhC microcavities is envisaged in Figure 21H, showcasing deformation-independent sensitivity to the ambient index variation [186]. Multiplexing has also been implemented for simultaneous detection of specific analytes [183, 187].

Cascaded PhC complexes for biosensing have been actualised (see Figure 22) insofar as high-density silicon-integrated microarrays, comprising 64 PhC microcavity sensors, were fabricated. It is pertinent to note that all of these PhCs can be interrogated at the same time for specific, label-free biodetection [183, 187]. In Figure 22F–I, multiple spectra were monitored for ZEB1 in lung cancer cell lysates with a 2D PhC array (~11-μm² surface area apiece) composed of four arms of multiplexed L13 microcavities coupled to respective W1 PhC waveguides [147]. In a given instance of time, this platform permits concurrent quantification of many binding interactions with distinct, immobilised antibodies from the same sample [147, 183, 187]. This group claims the detection of a single protein out of a complex mixture containing 20,000–50,000 proteins, proving the PhC microcavity's potential for point-of-care testing [147].

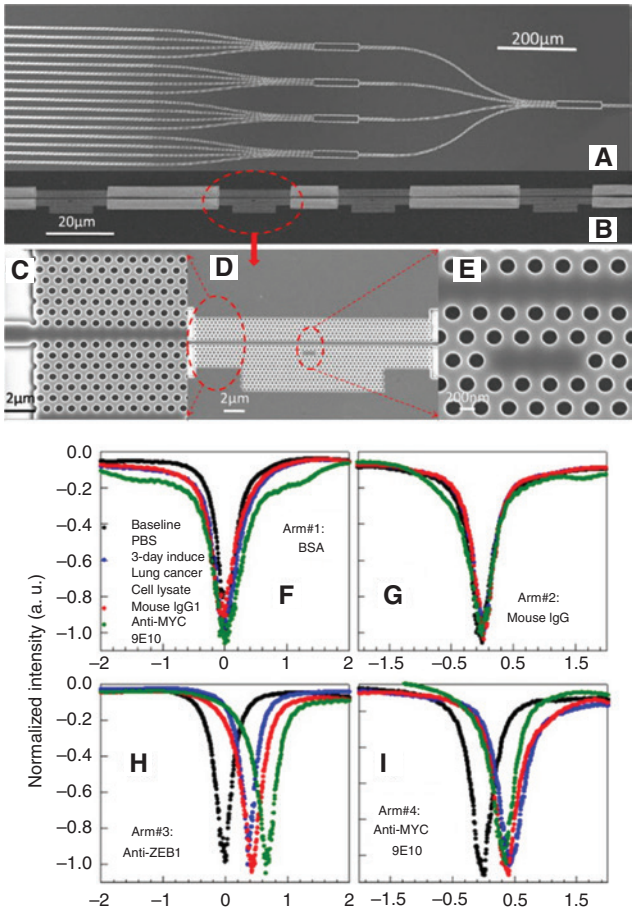

Figure 22: Multiplexed sensing with PhCs.
(A)–(E) SEM images of a multiplexed biosensing architecture with 16 arms of cascaded PhC microcavities. (A) is an image of the entire device, and (B) is that of an arm with four cascaded PhC microcavities. (C)–(E) are zoomed-in images of such a PhC microcavity, composed of an engineered L3 PhC microcavity two rows away from a W1 PhC waveguide. Adapted from [183] and [187]. (F)–(I) Simultaneous, specific detection of ZEB1 in lung cancer cell lysates with four arms of multiplexed L13 PhC microcavities coupled to their respective W1 PhC waveguides. The resonant wavelength positions for the base line (black), lung cancer cell lysates (red), mouse IgG1 (blue), and anti-MYC 9E10 (green). Adapted from [147].

Unlike engineered point defects with a smaller hole size as compared to the surrounding PhC holes for protein detection [137], virus-sized particle detection demands larger point defects in comparison to the surrounding holes [188]. PhC nanocavities were designed and adapted to integrated biosensing of virus-sized particles under microfluidic flow (Figure 23), wherein there is a large-defect W1 waveguide-coupled 2D PhC [149]. Integrated PhC platforms are well-suited for the on-chip optical trapping, assessment, and manipulation of micron-scale objects. Unlike conventional synthetic particles, living entities have a lower index contrast in aqueous media

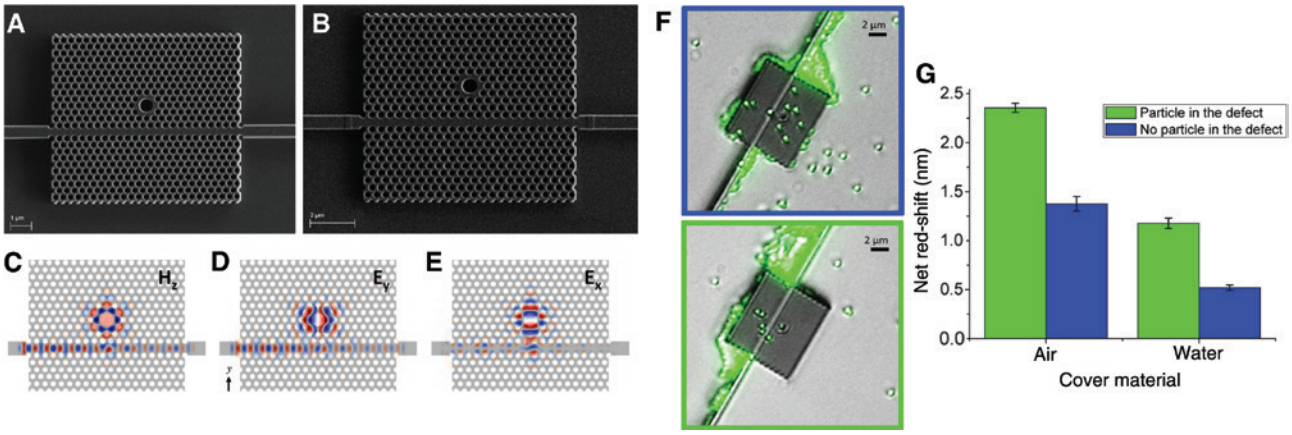

Figure 23: Photonic crystal nanocavities for biosensing of virus-sized particles under microfluidic flow.
(A) and (B) SEM micrograph of two PhC sensors consisting of a triangular lattice with a point-like defect centred four and five rows away from the waveguide, respectively. (C)–(E) Numerically simulated electromagnetic field profiles of the device showing field localisation about the engineered hole defect. (F) Fluorescence microscopy images of the PhC sensor in the presence and absence of the fluorescent latex microsphere with the large engineered hole defect. (G) Corresponding net red shifts of the optical resonance wavelength. Adapted from [149].

(e.g. water) and, generally, an inhomogeneous index distribution. The local enhancement of evanescent fields in PhC microcavities in SOI can serve as localised optical traps for bacteria as depicted in Figure 24 [145]. Glancing at Figure 24A, *Bacillus subtilis* and *Escherichia coli* bacteria were trapped with reportedly strong in-plane trap stiffnesses of ~7.6 pN/(nm · W) [145]. With this versatile approach, one can combine PhC microcavity-based biosensors with microfluidics in a scalable fashion to attain several parallel sensing/trapping sites in a microfluidic lab-on-a-chip [145].

Increasing the overlap between the optical field and target analyte is a notable challenge in the development of integrated optical biosensors. In slotted PhCs, an air-slot waveguide is engineered within a PhC to squeeze light into a miniscule volume of air, simultaneously exploiting the slot waveguide's spatial confinement as well as basic PhC-derived temporal confinement [141, 151–153]. From

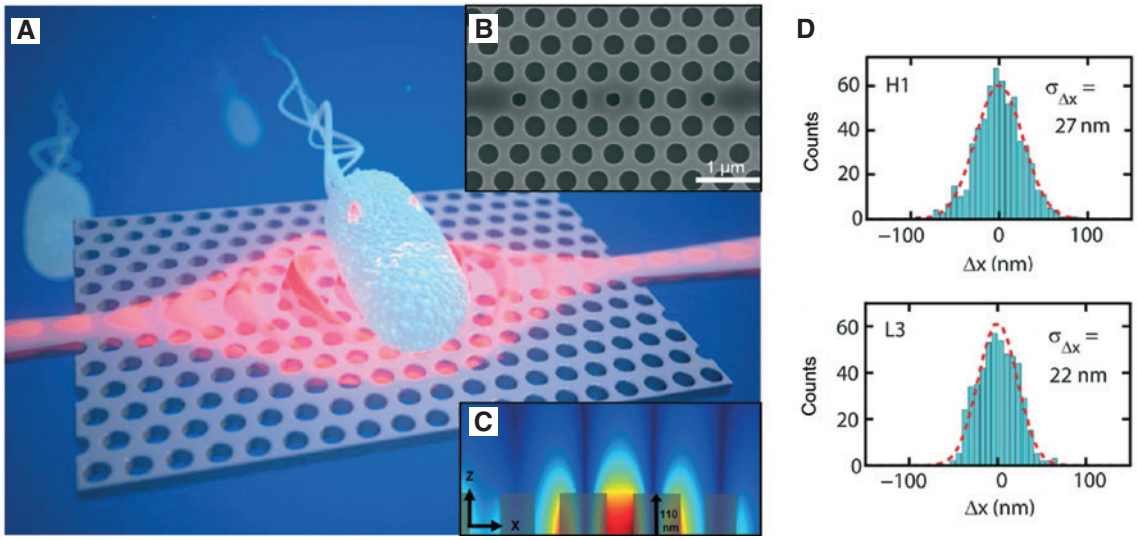

Figure 24: Photonic crystal microcavities as localised optical traps for bacteria.
(A) Artistic rendition of optical trapping of single bacteria using PhC cavities for local enhancement of the evanescent field. (B) SEM image of a H1 cavity in a PhC. The central hole is smaller than the regular holes and the adjacent ones are duly optimised. (C) Mode profile of the cavity. The amplitude of the electric field $|\vec{E}|$ is in the vertical plane through the central *x*-axis. (D) Histograms of the displacement of the trapped *B. subtilis* spore from the central position for different PhC cavities. Adapted from [145].

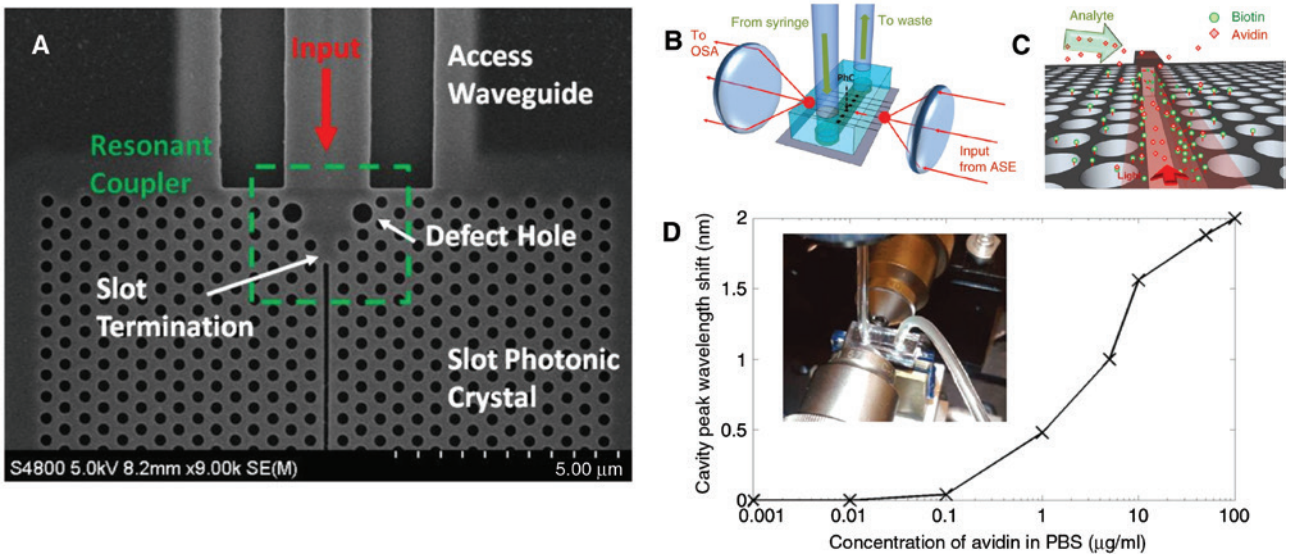

Figure 25: An example of a slotted PhC design.
(A) SEM image of a slotted PhC fabricated in an SOI wafer, with resonant defect couplers and access waveguides, and (B) schematic of the experimental setup. (C) Depiction of avidin binding to a biotin-coated slotted PhC biosensor and (D) the induced cavity peak wavelength shift (wherein the inset is the experimental arrangement for fluid injection into the slotted PhC chip). Adapted from [141] and [153].

the point of view of biosensing, this modality is envisaged to indeed have enhanced light-matter interactions and the required field overlap in the slot waveguide region. In Figure 25A, one of the fabricated slotted PhCs on SOI is shown. It is suitable for the spectral region of interest as well as for enhanced light coupling from the access waveguide. The schematic, experimental scheme using a biotin coating for detection of avidin, and the ensuing wavelength shift are given in Figure 25B–D.

It has been further numerically computed that an optimised combination of a passive PhC waveguide cavity and a nanoslot structure would strengthen the optical trapping gradient force by more than 10^3 times compared to conventional waveguide trapping [161]. A point defect-engineered active PhC cavity made of an emitting material such as III-V semiconductors can be used as a laser source [189, 190] and for exploring chemical analyses wherein adsorption induces a lasing spectral shift with a very narrow linewidth and high sensing resolution in comparison to the passive counterpart [191, 192]. For example, in Figure 26A and B, a typical nanoslot nanolaser is created within a single GaInAsP/InP quantum-well wafer with a total thickness of GaInAsP layers, including the quantum well, of ~180 nm [163, 192]. In the nanoslot region, the electric field vector $\vec{E}$ is primarily oriented normal to the sidewalls and, since the normal component of the displacement vector is continuous across the boundary, $\varepsilon|\vec{E}|^2$ could be increased inside the nanoslot by $\varepsilon'_{\text{Slot}}/\varepsilon_{\text{Environment}}$ where ε is the dielectric constant [192]. The drawing of the nanoslotted PhC nanolaser for biodetection and the experimental microscope setup are displayed in Figure 26A and B [166]. One of the fascinating features of these particular nanolasers is the possibility of dense integration to even more than 10,000 nanolasers in a ~1 mm^2 PhC slab [193]. Such an array of nanolasers is given in Figure 26C, while a schematic as well as sensing data for nanoslotted PhC nanolasers is found in Figure 26D–H [164, 167]. An ultralow detection limit of 16 zM was reported for a biotin coating in pure water with streptavidin (SA). Moreover, 100 zM SA protein in samples with 1-µm BSA contaminant was detected with a selectivity of 10^{13} [164].

Now, we will consider a special case of integrated PhC design for biodetection, viz., PhC nanobeam cavities. Unlike the PhC slab-based microcavity we have previously seen, the PhC nanobeam cavity, in general, comprises a ridge waveguide patterned with one line of PhC nanoholes tuned to obtain Bragg reflection for longitudinal confinement [140, 150, 194, 195]. The holes nearer to the centre of the nanobeam can be further tapered in order to reduce the transverse mode profile mismatch for better cancellation of out-of-plane radiation losses [194]. The optimal nanobeam cavity would facilitate truly large-scale integration – a critical requisite for new-age biosensors. Unlike the immobilisation of one or more active molecules, in Figure 27, an optical trap was employed to inspect free-solution interactions between a single H1N1 influenza virus and specific antibodies via their Brownian fluctuations [150]. The stoichiometry of the binding antibodies was estimated using their density and mass (see Figure 27D), showing that

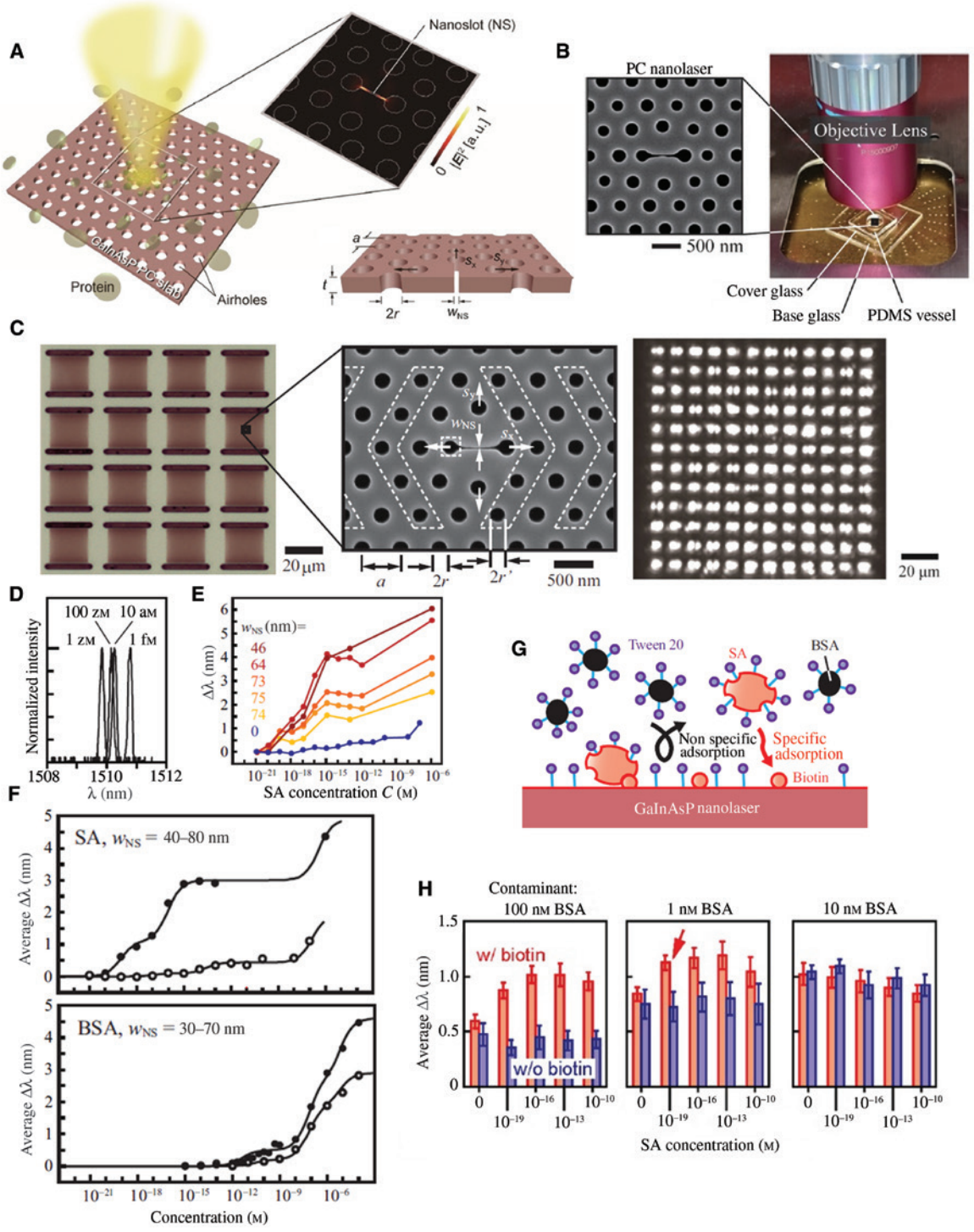

Figure 26: Nanoslot nanolasers in PhCs.
(A) Nanoslotted PhC nanolaser with adsorbing biomolecules, shown alongside a computed modal energy distribution (above) and cross-sectional schematic of the device (below). Adapted from [163]. (B) Experimental configuration, including an SEM image of a PhC sample, and (C) an array of nanoslotted GaInAsP PhC nanolasers for biosensing (i.e. optical micrograph to the left, SEM image of a subsection with modified side hole diameters in the centre, and near-field pattern of the 144-nanolaser array to the right). Adapted from [164, 166, 167]. (D) Laser spectra at different SA concentrations and (E) wavelength shift $\Delta\lambda$ versus SA concentration for six devices with varying nanoslot widths W_{NS}. (F) Average wavelength shift for devices with (closed circles) and without (open circles) a nanoslot. Adapted from [163] and [164]. (G) Pictorial representation of specific biotin-SA binding, in a BSA-contaminated environment, onto the nanoslotted PhC nanolaser biosensor. (H) Biosensing of SA protein in samples with BSA contaminant wherein the contaminant concentration increases from left to right. The error bars show a 95% confidence interval where the largest selectivity is indicated by the red arrow. Adapted from [165].

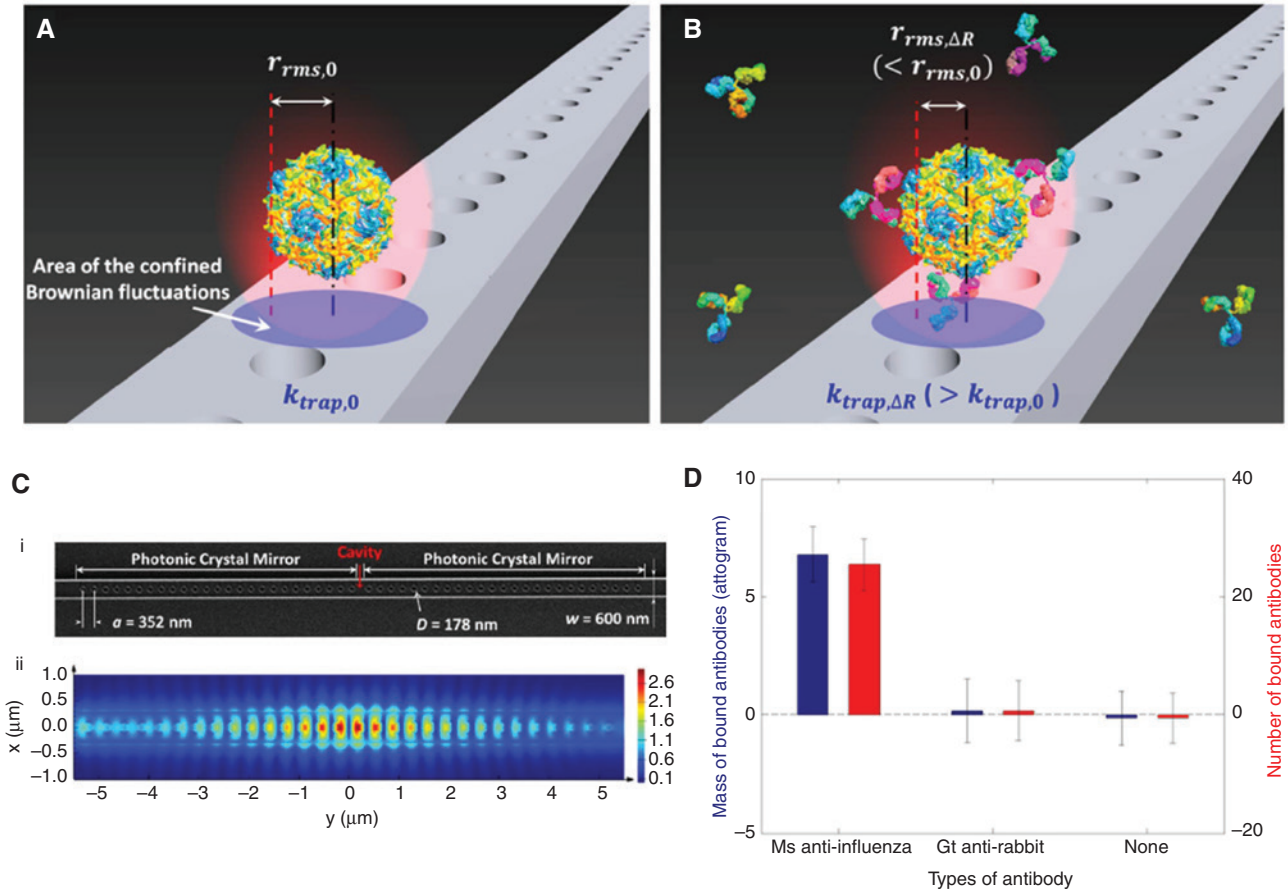

Figure 27: Optical trap to inspect interactions between a single H1N1 influenza virus and specific antibodies.
(A) and (B) Label-free detection of binding interactions between (A) a single influenza virus and (B) binding anti-influenza antibody in a nanophotonic near-field trap. The subscript 0 denotes an initial measurement and subscript ΔR denotes the measurement at equilibrium. Models from the Protein Data Bank Embedded Python Molecular Viewer open-source plug-in were used for the illustration. (C) SEM image of the nanobeam PhC resonator and computed strong field confinement within the resonator nanocavity in (C). (D) Stoichiometry of the studied binding antibodies using the density and mass of bound biomolecules. Adapted from [150].

the binding capacity of anti-influenza immunoglobulin G (IgG) antibodies to the virus was 6.8 ± 1.1 ag (26 ± 4 IgG) per H1N1 influenza virus [150].

Figure 28A–C are derived from a topical study on PhC nanobeam sensors operating inside a biological cell. The reported nanoprobe consists of a GaAs nanomembrane, 220 nm thick, containing three layers of high-density InAs quantum dots. On this template is the five-hole taper defect PhC nanobeam, epoxy bonded to the edge of a multimode optical fibre (Figure 28A and B). Basic function herein involves emitted photoluminescence from the embedded quantum dots and highly confined resonant modes sustained within the cells. These nanocavity probes allow for multi-faceted real-time biomarker detection inside living cells [154]. Going further, the optical trapping and spatio-temporal examination of a bacterium (e.g. *Staphylococcus epidermidis*, *E. coli*, and *B. subtilis*) is given in Figure 28D–F [146]. Individual planktonic cell bacteria can be trapped by the evanescent field of a properly tuned microcavity, spatially capturing morphological characteristics and temporally classifying the bacterial phenotype [146].

In the first few sections of our review, we had already looked at plasmonic nanostructures, their potential for sensing, and their role as a keystone in cutting-edge sensors that utilise WGM-LSPR hybridisation. Analogously, we will now delve into optoplasmonic platforms that incorporate PhC micro/nanocavities and plasmonics [170, 171]. It has been proposed that highly confined hybrid cavity modes can be generated by means of an optical nanocavity made up of PhCs coupled to a metal surface with a nanoscale air gap [196]. This method involves the hybridisation of PhC modes and surface plasmons across the air gap resulting in a deep subwavelength mode volume V and large quality factor Q, therefore equating to an impressively high Q/V [196]. Nanoarchitectures for redistributing the intrinsically evanescent SPP field

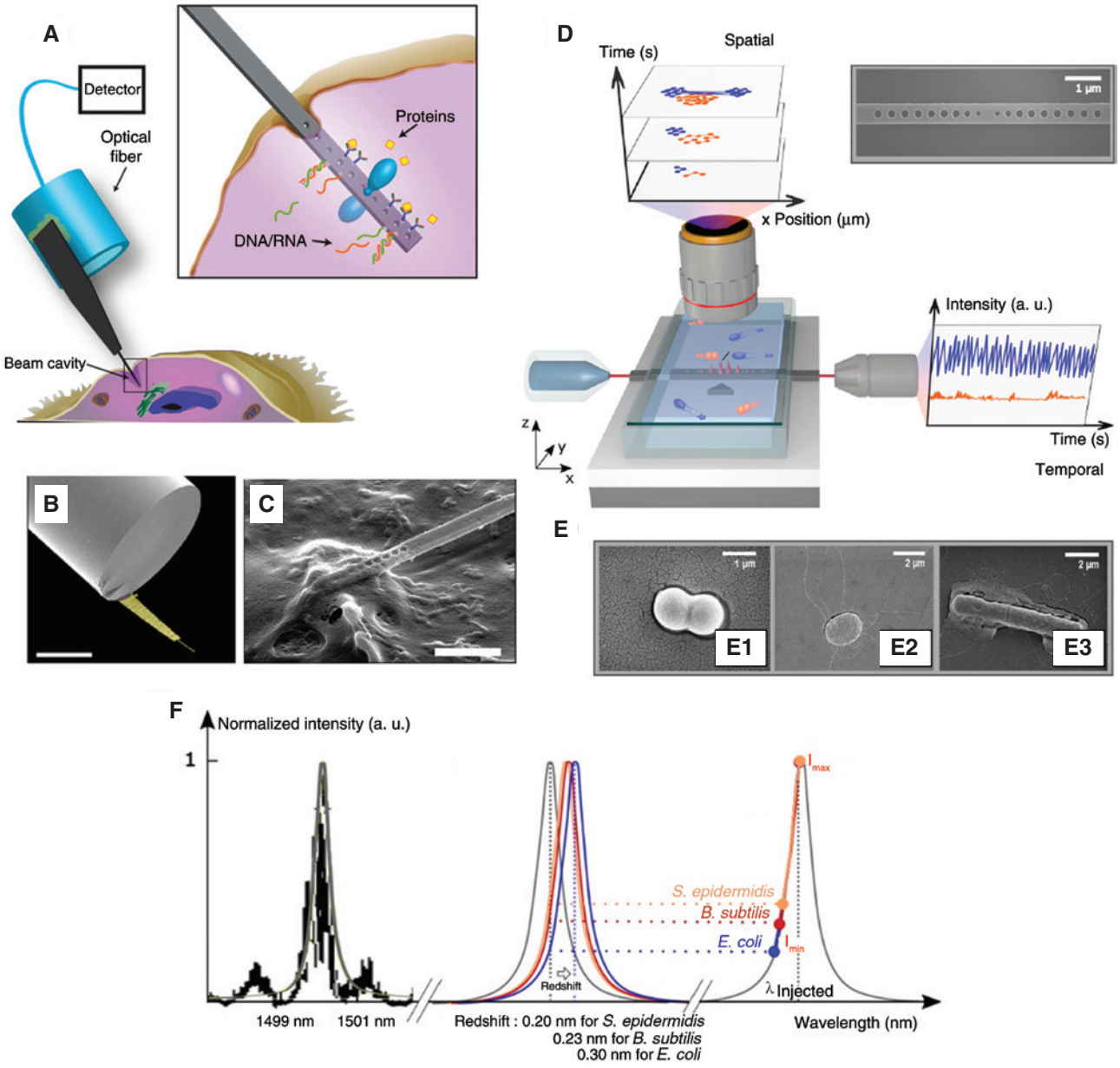

Figure 28: *In vivo* operation of photonic crystal nanobeam sensors.
(A) Diagram of the PhC nanobeam inserted into a cell, probing for DNA/RNA and proteins. (B) Pseudocoloured SEM image of a typical fabricated nanoprobe device (scale bar = 50 µm) and (C) an SEM image of a cell punctured by the nanobeam (scale bar = 2 µm). Adapted from [154]. (D) Spatio-temporal analysis of bacteria using the PhC nanobeam cavity optical trapping setup, measuring *E. coli* (in blue) and *S. epidermidis* (in orange). (E) SEM micrographs of the bacteria under study: diplococcus of *S. epidermidis* (E1), *E. coli* (E2), and aggregate of *B. subtilis* (E3). (F) Recorded resonance peak of the PhC nanobeam cavity (in black) together with its Lorentzian fit (in grey). The redshifts in the resonance wavelength due to close bacteria are outlined, as well as a representation of such a redshift in the resonance peak delineated segments for each of these bacteria. Adapted from [146].

to a propagating electromagnetic wave, which could be detectable through Raman scattering in the far field, have also emerged [170, 171]. These devices in question were analysed computationally and experimentally as can be seen in Figure 29.

The SEM micrograph of Figure 29A reveals a surface-enhanced, label-free nanosensor comprising an L3 cavity-embedded PhC with a plasmonic nanoantenna (2.5 µm high, with a base diameter = 90 nm gradually decreasing to a radius of curvature = 10 nm at the tip) at the centre [170]. Single inorganic nanoparticles and monolayers of organic compounds, e.g. benzenethiol (BTH), could be sensed. In a standard Raman configuration, the measured enhancement factor of the Raman signal with respect to a

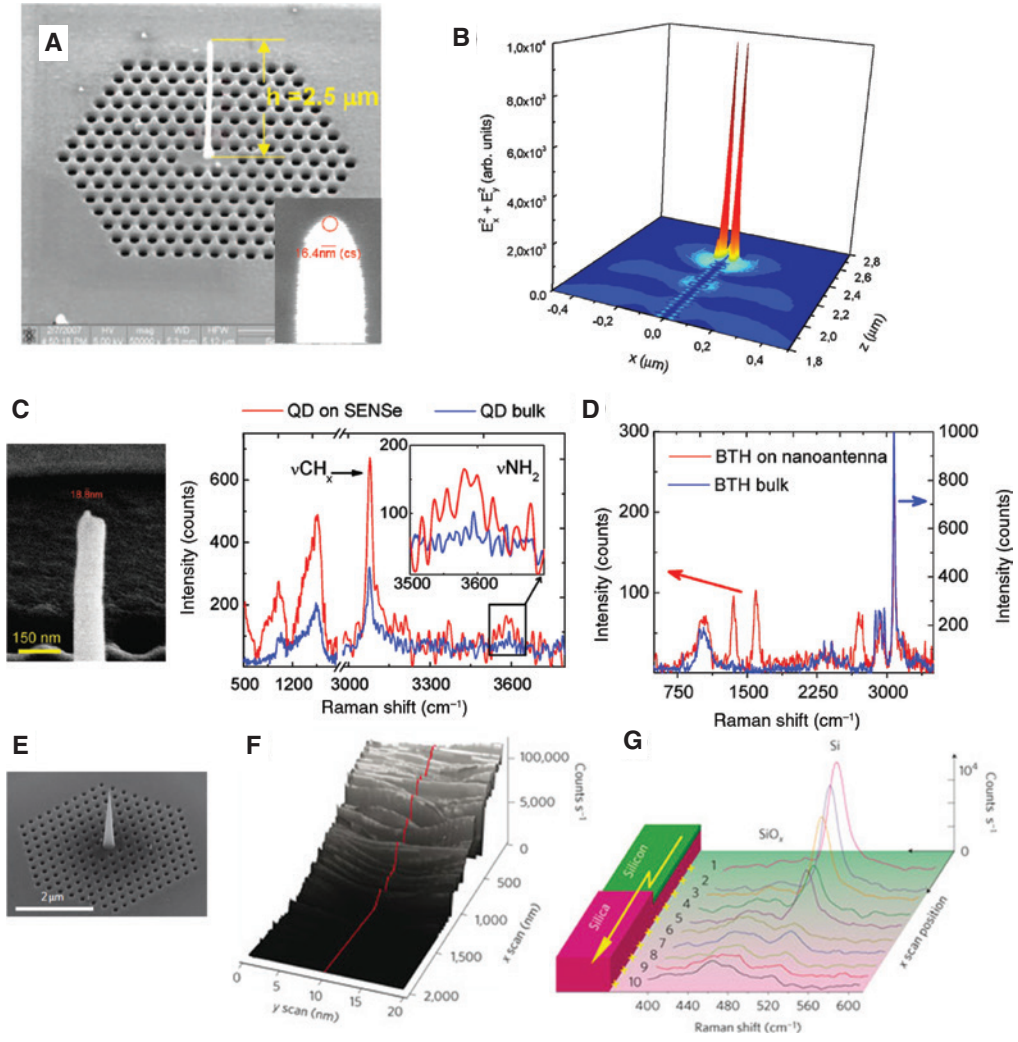

Figure 29: Photonic crystal nanosensor with a plasmonic nanoantenna.
(A) SEM micrograph of a surface-enhanced nanosensor with a plasmonic nanoantenna at the centre of an embedded PhC cavity. The inset is an enlarged view of the nanoantenna. (B) Simulated 3D intensity profile along the nanoantenna. (C) To the left is an SEM image of the plasmonic nanoantenna with a deposited core-shell ZnS/CdSe quantum dot at its tip, while to the right is a Raman spectrum taken from single (red) and bulk (blue) quantum dot samples. (D) Confocal Raman scattering measurements on the nanoantenna (red) compared to the bulk spectrum on the benzenethiol monolayer. Adapted from [170]. (E) SEM micrograph of a hybrid photonic-plasmonic nanodevice, i.e. a PhC cavity with a tapered metallic waveguide on an AFM cantilever. (F) and (G) wide-scan Raman spectra and 3D map of the silicon nanocrystal/SiO_x surface, respectively. Adapted from [171].

bulk BTH sample was approximately 3×10^6 with a detection limit between 10 and 250 molecules [170]. Going one step further, a 2D PhC cavity and tapered Ag waveguide on a Si_3N_4 AFM cantilever was reported [171]. This relies on the generation as well as localisation of SPPs for the topographic, chemical, and structural mapping of Si nanocrystals up to a spatial resolution of 7 nm [171].

Among various attempts to devise a hybrid photonic-plasmonic scheme with numerous geometries, Figure 30A and B are technical drawings and field profiles for a PhC nanobeam cavity with a gold bowtie nanoantenna [173]. Computational analysis pinpointed parameters/dimensions for an ultrahigh Q/V ratio and hence conditions conducive for trapping and micromanipulation. The experimental realisation of a hybrid nanolaser that uses the coupling between a LSPR of a bowtie and photonic mode of an active PhC with a L7 microcavity is visible in Figure 30C–H [179]. The fabrication approach is also flexible in terms of variability of scale and morphology as is demanded by the constraints imposed by the analyte.

A genuine lab-on-chip device, i.e. PhC slabs below bottom-up synthesised SERS nanocapsules with densely surface-distributed Ag nanoparticles, and its operation are laid out in Figure 31 [178]. In Figure 31C–F, we see that intriguing compounds such as adenine and melamine can

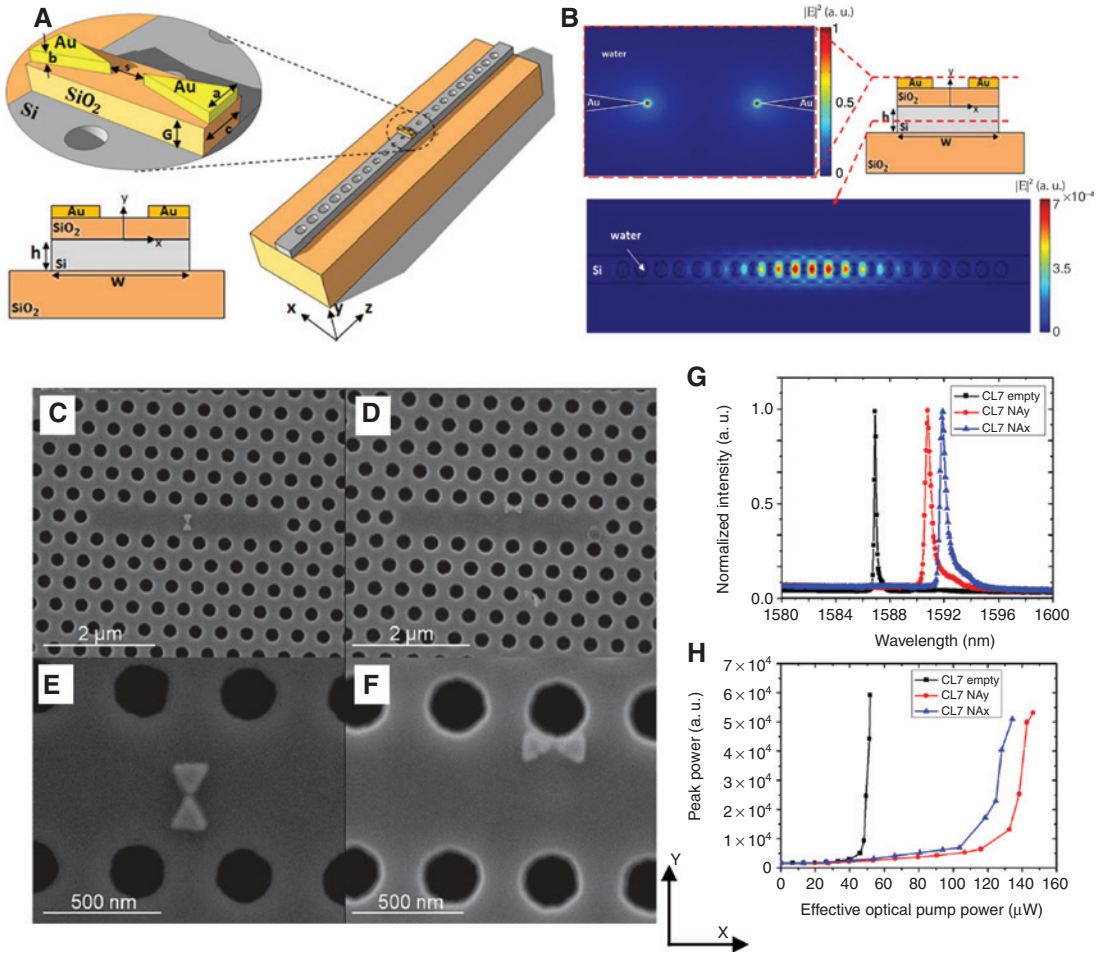

Figure 30: Photonic crystal nanobeam cavity with a gold bowtie nanoantenna.
(A) Hybrid photonic-plasmonic device configuration, featuring a gold plasmonic nanoantenna supported by a dielectric layer on a silicon PhC nanobeam cavity. (B) Computed relative intensity distribution at the surface of the bowtie (top) and in the PhC nanobeam (bottom). Adapted from [173]. (C)–(F) SEM images of a hybrid nanolaser encompassing a linear PhC microcavity and gold bowtie nanoantenna where (C) the nanoantenna is at the centre and (D) at the edge of the PhC microcavity. The respective magnified images are (E) and (F). (G) and (H) Performance characterisation of the hybrid nanolaser with and without the plasmonic nanostructure. Here, the (G) normalised lasing spectra and (H) peak versus optical pump power are plotted. Adapted from [179].

be precisely identified [178]. Lateral to this, 3D plasmonic metamaterials have been constructed from silver-coated 3D woodpile PhCs produced by multi-photon polymerisation (Figure 32A and B), exceeding spectral sensitivities of 2600 nm per refractive index unit. It is conceivable that these 3D metamaterials could be merged with more intricate 3D PBG cavities (Figure 32C) to ameliorate biodetection limits [197].

A few of the latest developments in hybrid photonic-plasmonic apparatuses, involving PhCs, have arrived at ascertaining single-molecule signatures [180–182]. Self-assembled silver nanoparticles on diatom PhC biosilica, visible in Figure 33, is a shining example [180]. SEM micrographs of a single diatom frustule (Figure 33A and B) and the deposited silver seeds (Figure 33D) can be seen, alongside a SERS spectrum (Figure 33E) for 2000 droplets of 10^{-16} M rhodamine 6G (cf. Figure 33C) dispensed via an inkjet printer [180].

One final technological innovation to consider is a PhC nanobeam with a spherical gold particle for real-time tracking of DNA-XPA (xeroderma pigmentosum complementation group A) dynamics (Figure 34) [182]. Liang et al. fashioned a single-molecule biosensor on SOI with a microfluidic chip, wherein the plasmonic resonator confines photons to a mode volume $\sim V = 3.5 \times 10^{-4}\ \lambda^3$ and the PhC alone has a $V = 0.1\ \lambda^3$. The gradient force generated by the PhC nanobeam is sufficient to trap the Au particle, exciting its LSPRs and maintaining slight separation in respect to the PhC nanobeam sidewall. Label-free tracking of resonance shifts brought about by single-molecule binding events is shown in Figure 34D–G, witnessing mismatched double-stranded DNA (dsDNA) and XPA in

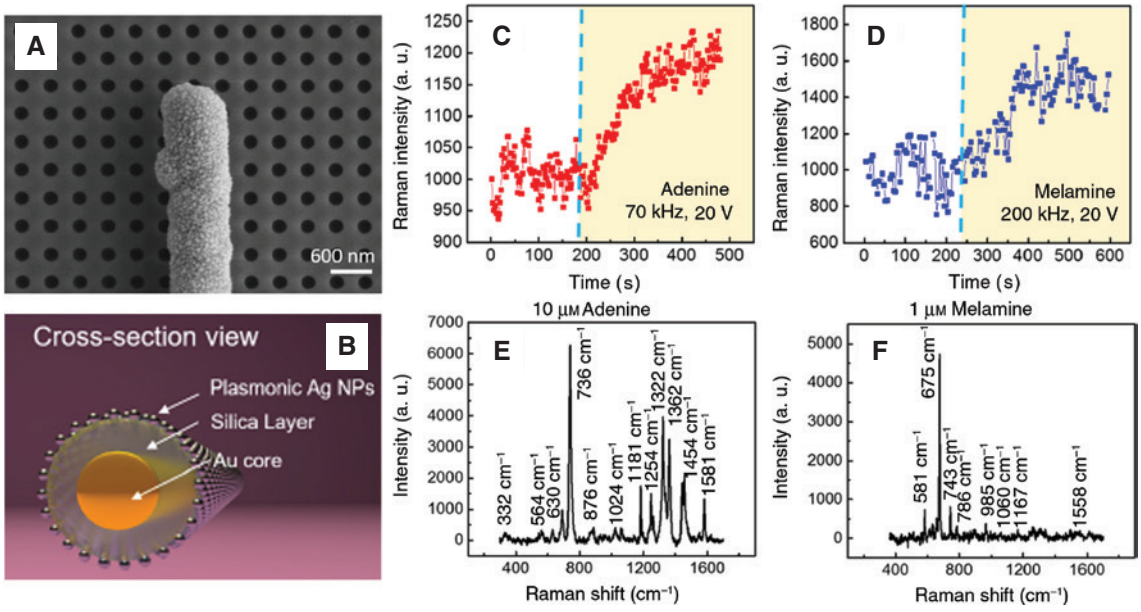

Figure 31: Integrated hybrid plasmonic-photonic architecture for electrokinetic manipulation and biochemical detection.
(A) SEM image of a nanocapsule aligned on lithographed nanophotonic crystals. (B) Cross-sectional view of the nanocapsule in which a metallic Au nanowire serves as the core; there is an intermediately grown silica layer, and plasmonic Ag nanoparticles are uniformly grown around it. (C)–(F) Time-dependent Raman intensity and full Raman spectrum, respectively, for (C) and (E) adenine and (D) and (F) melamine molecules. Adapted from [178].

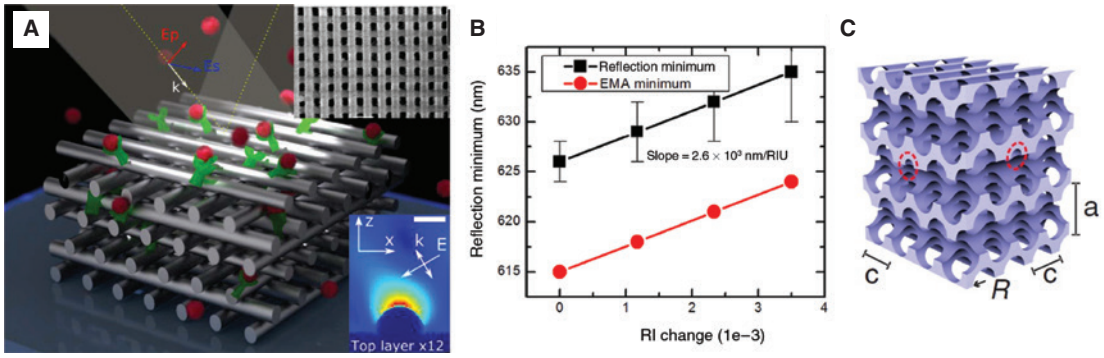

Figure 32: 3D plasmonic metamaterials and PBG cavities.
(A) Biosensing with a metamaterial, i.e. a silver-coated 3D woodpile PhC fabricated from photopolymerisable composite. The insets are an SEM image of the woodpile crystal (top) and a finite-difference time-domain simulation of the electric field distribution (bottom). (B) Measured and computed (with an effective medium approximation) spectral position of the reflection minimum for a refractive index change due to injection of varyingly concentrated glycerol. Adapted from [175]. (C) Oblique view of a modelled 3D inverse woodpile PhC with a point defect, resulting in a 3D PBG cavity. R is the bulk radius of the pores, while a and c are orthorhombic lattice parameters. The red circles indicate two smaller pores with a radius $R' = 0.5R$. Adapted from [197].

Figure 34D and E as well as normal dsDNA and XPA in Figure 34F and G [182].

5 Outlook

While the possible geometries of plasmonic materials developed in diverse directions and were optimised for specific measurement tasks, the types of materials used are still limited. New material combinations and single-particle engineering will provide sensing capabilities where pure gold and silver cannot be applied, e.g. as in the case of unwanted side reactions or lower enhancement. This similarly applies to the surface chemistry of the sensors. Though manifold protocols exist to modify noble metals and other plasmonic materials, they are

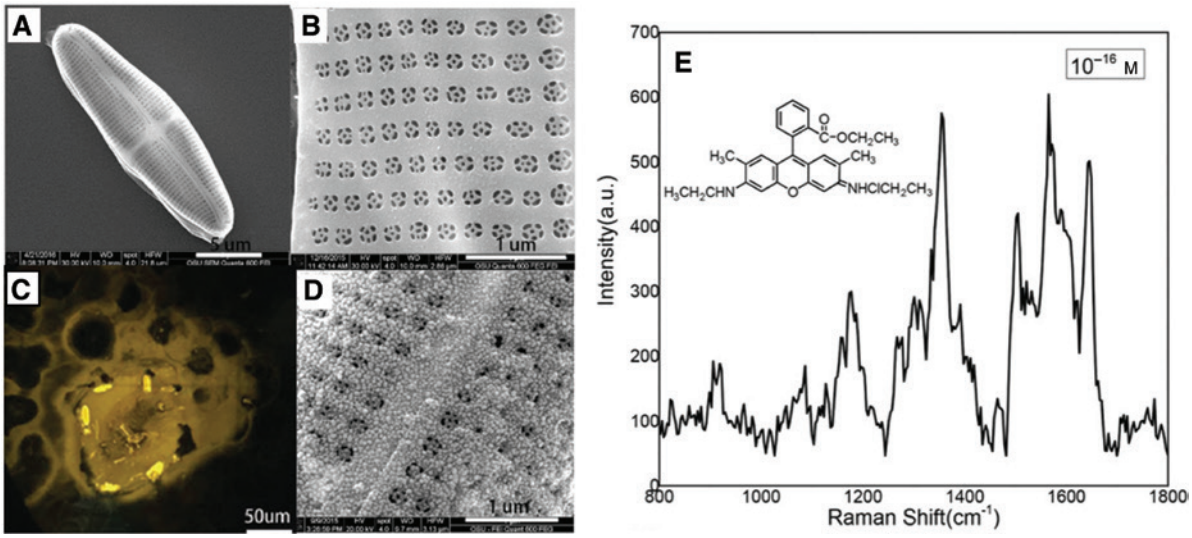

Figure 33: A single-molecule biosensor comprising self-assembled silver nanoparticles on photonic-crystal-like diatom biosilica. (A), (B), and (D) SEM visualisation of (A) a single diatom frustule (*Pinnularia*) harbouring (B) arrays of pores and (D) silver seeds deposited onto it. (C) 200 fluorescent droplets (20 nl) of aqueous R6G solution (10^{-7} M) displayed on the device, as well as (E) the SERS spectrum of 2000 droplets at 10^{-16} M exhibiting extraordinary sensitivity. Adapted from [180].

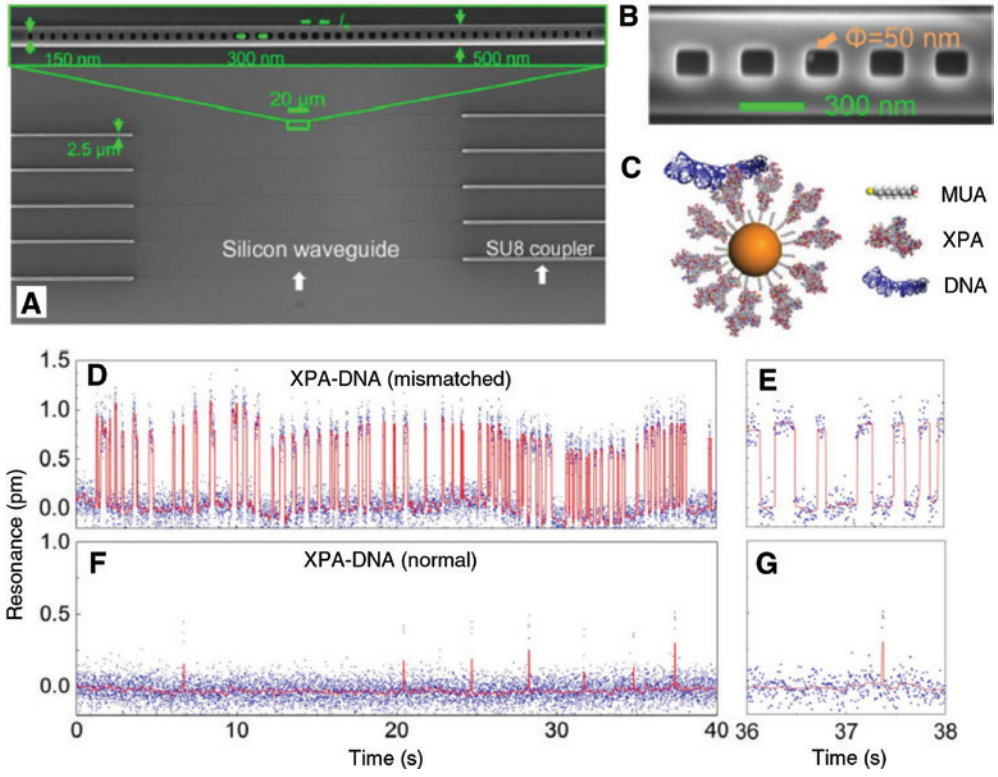

Figure 34: Real-time monitoring of single DNA-XPA dynamics with a hybrid system.
There is an SEM picture of (A) multiplexed PhC nanobeam cavities together with the waveguiding components for input/output coupling and (B) the gold nanoparticle trapped within. An orange arrow points to the 50-nm diameter Au particle in the central grating. (C) Biofunctionalisation of the Au nanoparticle, immobilising XPA proteins on a self-assembled monolayer of 11-mercaptoundecanoic acid (11-MUA) attached to the Au and which interacts with the dsDNA. (D)–(G) Resonance signal tracking in real time, revealing binding dynamics of (D) and (E) mismatched dsDNA and XPA in standard binding buffer (dsDNA concentration = 10 nM), as well as (F) and (G) normal dsDNA and XPA serving as a control. Adapted from [182].

still often based on standard random conjugation strategies. In the future, it will be possible to control the site-specific placement of the molecules at nanometer-precise positions within the electromagnetic field, e.g. mechanically or by plasmon-catalysed reactions and in optimal sensing orientations. Sensing of multiple parameters in complex biological environments was enabled by some plasmon-based sensors [37, 98, 198, 199], and, given time, such techniques will develop further for analyses in the environments that are demanded by biosensing. The integration and combination of plasmonic nanostructures with components for trapping, detection, and excitation sources on miniaturised platforms will thus help in performing *in situ* or even *in vivo* analyses.

Optoplasmonic systems based on high-Q nano/microcavities and small modal volumes with metal nanoparticles and nanostructures allow for high Q/V sensor systems that realise new functionalities and detection modalities. The combined system exhibits a comparatively high Q-factor via the nano/microcavity, combined with a small modal volume and high near-field enhancements via the plasmonic nanostructure. This combination and the high Q/V ratio directly results in improved sensitivity, enabling single-molecule detection and single-ion sensing.

Both underpinning technologies, high-Q optical nano/microcavities and plasmonic entities, have been developed for quite some time and have been realised in various sensing geometries and materials. Ideal combinations will have to be found, where particularly advances in the control of nanoparticle fabrication and positioning as well as design and fabrication of high-Q nano/microcavities will aid in the process. Recent advances in nanotechnology provide the possibility to fabricate resonator structures on the micron- to nanoscale, from different optical materials and using a host of different fabrication techniques, and to control the assembly and integration of hybrid sensor structures. Applying these methods to the hybrid sensor system to tune the properties of the combined system will provide unique sensing capabilities for specific applications. The hybrid sensor system already exhibits unprecedented sensitivity for label-free detection of biological and chemical entities in the optical domain. Further improvements towards ultimate sensitivities will not only enable sensor systems that can probe unique optical and material properties at the single-molecule level, but also provide unique physical properties that in return may push the detection envelope. An example of this is the use of backaction by molecular springs to enhance a single-molecule Raman signal. Further advantages of the hybrid system are given by the coupling and decoupling of plasmonic nanoparticles to the nano/microcavity, thereby preserving particle mobility and diffusion limits in sensing. Furthermore, a highly-multiplexed system with many plasmonic nanoparticles combined with a nano/microcavity structure could be integrated onto lab-on-chip devices, wherein the multiplexed sensors may achieve lower detected concentration limits. A hybrid sensor could be probed with different laser sources to probe different characteristics of the same molecule. As the system matures, it should soon become a tool to fully characterise molecules. Realising such a "molecule scanner" has been the dream of biochemists, biotechnologists, and physicists alike. In light-matter interactions, such molecular scanners may also provide near-field enhancements for studies of nonlinearities with reduced thresholds. Nonlinear species could be more easily probed this way, also permitting nonlinear processes to be exploited for novel applications.

Several challenges inhibiting the advancement of optoplasmonic systems exist. One is the mastery of controlled coupling of the sensor subsystems as to optimise all coupling parameters. Novel approaches must be developed to overcome the drawbacks of self-assembly of hybrid sensor structures or the high precision that is required for mechanical positioning of a plasmonic nanoparticle or nanostructure onto an optical nano/microcavity. Applications in sensing will require the mastery of surface functionalisation and the control of molecules and their precise attachments. The perhaps most challenging task will be the transformation of the hybrid system into an *in vivo* sensor, operating in complex environments as to fully characterise different molecules at the single-molecule level. *In vivo* as well as *in vitro* platforms could include planar silicon PhCs [127, 179, 182, 183, 193, 196] lying in the near-infrared part of the spectrum, potentially far-detuned from plasmon resonance [182]. Taking advantage of strong photon localisation and their simple design [128, 130, 134, 183, 196], the implantation of these sensors in living organisms could be feasible.

Lastly, optoplasmonic sensor systems will enable us to study the machinery of life: the functional movements associated with the activity of enzymes (including their subdomains) and all the other various functions that we observe for motor proteins, membrane receptors, etc. Hybrid sensors may add the fourth dimension to structural biology and represent the first optical technology capable of studying single-molecule protein dynamics without the need to label. Conformational transitions have already been highlighted for polymerase species, i.e. the Klenow fragment of *E. coli*, *Thermus aquaticus*, and *Pyrococcus furiosus* DNA polymerases [114]. Observing protein dynamics with hybrid sensors can add important

information to the dynamical studies of labelled proteins with established techniques such as Förster resonance energy transfer. Hybrid sensors may yet further harness the extreme speed, selectivity, and specificity of the nanoworld, for instance, in real-time single-molecule sequencing applications.

Acknowledgments: J. X., S. V., and F. V. acknowledge financial support from the Living Systems Institute, University of Exeter. They also, along with F. M., acknowledge support from the Max Planck Society.

References

[1] Vollmer F, Braun D, Libchaber A, Khoshsima M, Teraoka I, Arnold S. Protein detection by optical shift of a resonant microcavity. Appl Phys Lett 2002;80:4057–9.
[2] Arnold S, Khoshsima M, Teraoka I, Holler S, Vollmer F. Shift of whispering-gallery modes in microspheres by protein adsorption. Opt Lett 2003;28:272–4.
[3] Baaske MD, Foreman MR, Vollmer F. Single-molecule nucleic acid interactions monitored on a label-free microcavity biosensor platform. Nat Nanotechnol 2014;9:933–9.
[4] Foreman MR, Jin WL, Vollmer F. Optimizing detection limits in whispering gallery mode biosensing. Opt Express 2014;22:5491–511.
[5] Ament I, Prasad J, Henkel A, Schmachtel S, Sonnichsen C. Single unlabeled protein detection on individual plasmonic nanoparticles. Nano Lett 2012;12:1092 – 5.
[6] Zijlstra P, Paulo PMR, Orrit M. Optical detection of single non-absorbing molecules using the surface plasmon resonance of a gold nanorod. Nat Nanotechnol 2012;7:379–82.
[7] Anker JN, Hall WP, Lyandres O, Shah NC, Zhao J, Van Duyne RP. Biosensing with plasmonic nanosensors. Nat Mater 2008;7:442–53.
[8] Zhang WH, Martin OJF. A universal law for plasmon resonance shift in biosensing. ACS Photonics 2015;2:144–50.
[9] Yang J, Giessen H, Lalanne P. Simple analytical expression for the peak-frequency shifts of plasmonic resonances for sensing. Nano Lett 2015;15:3439–44.
[10] Miller MM, Lazarides AA. Sensitivity of metal nanoparticle surface plasmon resonance to the dielectric environment. J Phys Chem B 2005;109:21556–65.
[11] Jeong HH, Mark AG, Alarcon-Correa M, et al. Dispersion and shape engineered plasmonic nanosensors. Nat Commun 2016;7:11331.
[12] Saha K, Agasti SS, Kim C, Li XN, Rotello VM. Gold nanoparticles in chemical and biological sensing. Chem Rev 2012;112:2739–79.
[13] Tan SJ, Campolongo MJ, Luo D, Cheng WL. Building plasmonic nanostructures with DNA. Nat Nanotechnol 2011;6:268–76.
[14] Benz F, Schmidt MK, Dreismann A, et al. Single-molecule optomechanics in “picocavities”. Science 2016;354:726–9.
[15] Brolo AG. Plasmonics for future biosensors. Nat Photonics 2012;6:709–13.
[16] Kauranen M, Zayats AV. Nonlinear plasmonics. Nat Photonics 2012;6:737–48.
[17] Li M, Cushing SK, Wu NQ. Plasmon-enhanced optical sensors: a review. Analyst 2015;140:386–406.
[18] Lal S, Link S, Halas NJ. Nano-optics from sensing to waveguiding. Nat Photonics 2007;1:641–8.
[19] Liu N, Tang ML, Hentschel M, Giessen H, Alivisatos AP. Nanoantenna-enhanced gas sensing in a single tailored nanofocus. Nat Mater 2011;10:631–6.
[20] Wertz E, Isaacoff BP, Flynn JD, Biteen JS. Single-molecule super-resolution microscopy reveals how light couples to a plasmonic nanoantenna on the nanometer scale. Nano Lett 2015;15:2662–70.
[21] Guo LH, Jackman JA, Yang HH, Chen P, Cho NJ, Kim DH. Strategies for enhancing the sensitivity of plasmonic nanosensors. Nano Today 2015;10:213–39.
[22] Goncalves MR. Plasmonic nanoparticles: fabrication, simulation and experiments. J Phys D: Appl Phys 2014;47:213001.
[23] Kuhlicke A, Schietinger S, Matyssek C, Busch K, Benson O. In situ observation of plasmon tuning in a single gold nanoparticle during controlled melting. Nano Lett 2013;13:2041–6.
[24] Niu WX, Chua YAA, Zhang WQ, Huang HJ, Lu XM. Highly symmetric gold nanostars: crystallographic control and surface-enhanced Raman scattering property. J Am Chem Soc 2015;137:10460–3.
[25] Scarabelli L, Coronado-Puchau M, Giner-Casares JJ, Langer J, Liz-Marzan LM. Monodisperse gold nanotriangles: size control, large-scale self-assembly, and performance in surface-enhanced Raman scattering. ACS Nano 2014;8:5833–42.
[26] Genc A, Patarroyo J, Sancho-Parramon J, Bastus NG, Puntes V, Arbiol J. Hollow metal nanostructures for enhanced plasmonics: synthesis, local plasmonic properties and applications. Nanophotonics 2017;6:193–213.
[27] Ye XC, Gao YZ, Chen J, Reifsnyder DC, Zheng C, Murray CB. Seeded growth of monodisperse gold nanorods using bromide-free surfactant mixtures. Nano Lett 2013;13:2163–71.
[28] Sun HT, Sun X, Yu MP, Mishra AK, Huang LP, Lian J. Silica-gold core-shell nanosphere for ultrafast dynamic nanothermometer. Adv Funct Mater 2014;24:2389–95.
[29] Hong S, Lee MY, Jackson AO, Lee LP. Bioinspired optical antennas: gold plant viruses. Light Sci Appl 2015;4:e267.
[30] Chirumamilla M, Toma A, Gopalakrishnan A, et al. 3D nanostar dimers with a sub-10-nm gap for single-/few- molecule surface-enhanced Raman scattering. Adv Mater 2014;26:2353–8.
[31] Cui AJ, Liu Z, Li JF, et al. Directly patterned substrate-free plasmonic “nanograter” structures with unusual Fano resonances. Light Sci Appl 2015;4:e308.
[32] Cetin AE, Altug H. Fano resonant ring/disk plasmonic nanocavities on conducting substrates for advanced biosensing. ACS Nano 2012;6:9989–95.
[33] Wu CH, Khanikaev AB, Adato R, et al. Fano-resonant asymmetric metamaterials for ultrasensitive spectroscopy and identification of molecular monolayers. Nat Mater 2012;11:69–75.
[34] Al Balushi AA, Gordon R. Label-free free-solution single-molecule protein small molecule interaction observed by double-nanohole plasmonic trapping. ACS Photonics 2014;1:389–93.
[35] Lee KS, El-Sayed MA. Gold and silver nanoparticles in sensing and imaging: sensitivity of plasmon response to size, shape, and metal composition. J Phys Chem B 2006;110:19220–5.

[36] Genc A, Patarroyo J, Sancho-Parramon J, et al. Tuning the plasmonic response up: hollow cuboid metal nanostructures. ACS Photonics 2016;3:770–9.
[37] Govan J, Gun'ko YK. Recent progress in chiral inorganic nanostructures. Nanoscience 2016;3:1–30.
[38] Patra PP, Chikkaraddy R, Tripathi RPN, Dasgupta A, Kumar GVP. Plasmofluidic single-molecule surface-enhanced Raman scattering from dynamic assembly of plasmonic nanoparticles. Nat Commun 2014;5:4357.
[39] Kasera S, Biedermann F, Baumberg JJ, Scherman OA, Mahajan S. Quantitative SERS using the sequestration of small molecules inside precise plasmonic nanoconstructs. Nano Lett 2012;12:5924–8.
[40] Zhu WQ, Crozier KB. Quantum mechanical limit to plasmonic enhancement as observed by surface-enhanced Raman scattering. Nat Commun 2014;5:5228.
[41] Yampolsky S, Fishman DA, Dey S, et al. Seeing a single molecule vibrate through time-resolved coherent anti-Stokes Raman scattering. Nat Photonics 2014;8:650–6.
[42] Lee JH, Nam JM, Jeon KS, et al. Tuning and maximizing the single-molecule surface-enhanced Raman scattering from DNA-tethered nanodumbbells. ACS Nano 2012;6:9574–84.
[43] Langer J, Novikov SM, Liz-Marzan LM. Sensing using plasmonic nanostructures and nanoparticles. Nanotechnology 2015;26:322001.
[44] Luk'yanchuk B, Zheludev NI, Maier SA, et al. The Fano resonance in plasmonic nanostructures and metamaterials. Nat Mater 2010;9:707–15.
[45] Hsu MF, Nikolaides MG, Dinsmore AD, et al. Self-assembled shells composed of colloidal particles: fabrication and characterization. Langmuir 2005;21:2963–70.
[46] Pang YJ, Gordon R. Optical trapping of a single protein. Nano Lett 2012;12:402–6.
[47] Wheaton S, Gelfand RM, Gordon R. Probing the Raman-active acoustic vibrations of nanoparticles with extraordinary spectral resolution. Nat Photonics 2015;9:68–72.
[48] Xu HT, Jones S, Choi BC, Gordon R. Characterization of individual magnetic nanoparticles in solution by double nanohole optical tweezers. Nano Lett 2016;16:2639–43.
[49] Belkin M, Chao SH, Jonsson MP, Dekker C, Aksimentiev A. Plasmonic nanopores for trapping, controlling displacement, and sequencing of DNA. ACS Nano 2015;9:10598–611.
[50] Li N, Tittl A, Yue S, et al. DNA-assembled bimetallic plasmonic nanosensors. Light Sci Appl 2014;3:e226.
[51] Chen PC, Liu XL, Hedrick JL, et al. Polyelemental nanoparticle libraries. Science 2016;352:1565–9.
[52] Ye XC, Chen J, Diroll BT, Murray CB. Tunable plasmonic coupling in self-assembled binary nanocrystal super lattices studied by correlated optical microspectrophotometry and electron microscopy. Nano Lett 2013;13:1291–7.
[53] Chen HY, Lin MH, Wang CY, Chang YM, Gwo S. Large-scale hot spot engineering for quantitative SERS at the single-molecule scale. J Am Chem Soc 2015;137:13698–705.
[54] Cortie MB, McDonagh AM. Synthesis and optical properties of hybrid and alloy plasmonic nanoparticles. Chem Rev 2011;111:3713–35.
[55] Thacker VV, Hermann LO, Sigle DO, et al. DNA origami based assembly of gold nanoparticle dimers for surface-enhanced Raman scattering. Nat Commun 2014;5:3448.
[56] Nam S, Choi I, Fu CC, et al. Graphene nanopore with self-aligned plasmonic optical antenna. Biophys J 2014;106:414A.
[57] Burrows ND, Lin W, Hinman JG, et al. Surface chemistry of gold nanorods. Langmuir 2016;32:9905–21.
[58] Heucke SF, Baumann F, Acuna GP, et al. Placing individual molecules in the center of nanoapertures. Nano Lett 2014;14:391–5.
[59] Tan SF, Wu L, Yang JKW, Bai P, Bosman M, Nijhuis CA. Quantum plasmon resonances controlled by molecular tunnel junctions. Science 2014;343:1496–9.
[60] Kleemann ME, Mertens J, Zheng X, et al. Revealing nanostructures through plasmon polarimetry. ACS Nano 2016;11:850–5.
[61] Acimovic SS, Ortega MA, Sanz V, et al. LSPR chip for parallel, rapid, and sensitive detection of cancer markers in serum. Nano Lett 2014;14:2636–41.
[62] Bermúdez-Ureña E, Tutuncuoglu G, Cuerda J, et al. Plasmonic waveguide-integrated nanowire laser. Nano Lett 2017;17:747–54.
[63] Lin S, Crozier KB. Trapping-assisted sensing of particles and proteins using on-chip optical microcavities. ACS Nano 2013;7:1725–30.
[64] Trichet AAP, Dolan PR, James D, Hughes GM, Valiance C, Smith JM. Nanoparticle trapping and characterization using open microcavities. Nano Lett 2016;16:6172–7.
[65] Vahala KJ. Optical microcavities, Nature 2003;424:839–46.
[66] Foreman MR, Swain JD, Vollmer F. Whispering gallery mode sensors. Adv Opt Photonics 2015;7:168–240.
[67] Lee H, Chen T, Li J, et al. Chemically etched ultrahigh-Q wedge-resonator on a silicon chip. Nat Photonics 2012;6:369–73.
[68] Grudinin IS, Ilchenko VS, Maleki L. Ultrahigh optical Q factors of crystalline resonators in the linear regime. Phys Rev A 2006;74:063806.
[69] Gorodetsky ML, Savchenkov AA, Ilchenko VS. Ultimate Q of optical microsphere resonators. Opt Lett 1996;21:453–5.
[70] Iqbal M, Gleeson MA, Spaugh B, et al. Label-free biosensor arrays based on silicon ring resonators and high-speed optical scanning instrumentation. IEEE J Sel Top Quantum Electron 2010;16:654–61.
[71] Reed GT, Mashanovich G, Gardes FY, Thomson DJ. Silicon optical modulators. Nat Photonics 2010;4:518–26.
[72] Armani DK, Kippenberg TJ, Spillane SM, Vahala KJ. Ultra-high-Q toroid microcavity on a chip. Nature 2003;421:925–8.
[73] Shen BQ, Yu XC, Zhi YY, et al. Detection of single nanoparticles using the dissipative interaction in a high-Q microcavity. Phys Rev Applied 2016;5:024011.
[74] Hu YW, Shao LB, Arnold S, Liu YC, Ma CY, Xiao YF. Mode broadening induced by nanoparticles in an optical whispering-gallery microcavity. Phys Rev A 2014;90:043847.
[75] Shao LB, Jiang XF, Yu XC, et al. Detection of single nanoparticles and lentiviruses using microcavity resonance broadening. Adv Mater 2013;25:5616–20.
[76] Zhu JG, Ozdemir SK, Xiao YF, et al. On-chip single nanoparticle detection and sizing by mode splitting in an ultrahigh-Q microresonator. Nat Photonics 2010;4:46–9.
[77] Zhu JG, Ozdemir SK, He LA, Chen DR, Yang L. Single virus and nanoparticle size spectrometry by whispering-gallery-mode microcavities. Opt Express 2011;19:16195–206.
[78] Kim W, Ozdemir SK, Zhu JG, He LA, Yang L. Demonstration of mode splitting in an optical microcavity in aqueous environment. Appl Phys Lett 2010;97:071111.

[79] He LN, Ozdemir SK, Zhu JG, Yang L. Ultrasensitive detection of mode splitting in active optical microcavities. Phys Rev A 2010;82:053810.
[80] He LN, Ozdemir SK, Zhu JG, Kim W, Yang L. Detecting single viruses and nanoparticles using whispering gallery microlasers. Nat Nanotechnol 2011;6:428–32.
[81] Li BB, Clements WR, Yu XC, Shi KB, Gong QH, Xiao YF. Single nanoparticle detection using split-mode microcavity Raman lasers. Proc Natl Acad Sci USA 2014;111:14657–62.
[82] Ozdemir SK, Zhu JG, Yang X, et al. Highly sensitive detection of nanoparticles with a self-referenced and self-heterodyned whispering-gallery Raman microlaser. Proc Natl Acad Sci USA 2014;111:E3836–44.
[83] Ballard Z, Baaske MD, Vollmer F. Stand-off biodetection with free-space coupled asymmetric microsphere cavities. Sensors 2015;15:8968–80.
[84] Zhang SX, Wang L, Li ZY, Li Y, Gong QH, Xiao YF. Free-space coupling efficiency in a high-Q deformed optical microcavity. Opt Lett 2016;41:4437–40.
[85] Rosenblum S, Lovsky Y, Arazi L, Vollmer F, Dayan B. Cavity ring-up spectroscopy for ultrafast sensing with optical microresonators. Nat Commun 2015;6:6788.
[86] Kuo PS, Bravo-Abad J, Solomon GS. Second-hamonic generation using -quasi-phasematching in a GaAs whispering-gallery-mode microcavity. Nat Commun 2014;5:3109.
[87] Khanaliloo B, Mitchell M, Hryciw AC, Barclay PE. High-Q/V monolithic diamond microdisks fabricated with quasi-isotropic etching. Nano Lett 2015;15:5131–6.
[88] Chen R, Gupta S, Huang YC, et al. Demonstration of a Ge/GeSn/Ge quantum-well microdisk resonator on silicon:enabling high-quality GeSn; materials for micro- and nanophotonics. Nano Lett 2013;14:37–43.
[89] Lin JT, Xu YX, Fang ZW, et al. Fabrication of high-Q lithium niobate microresonators using femtosecond laser micromachining. Sci Rep 2015;5:8072.
[90] Haigh JA, Nunnenkamp A, Ramsay AJ, Ferguson AJ. Triple-resonant brillouin light scattering in magneto-optical cavities. Phys Rev Lett 2016;117:133602.
[91] Sedlmeir F, Zelter R, Leuchs G, Schwefel HGL. High-Q MgF_2 whispering gallery mode resonators for refractometric sensing in aqueous environment. Opt Express 2014;22:30934–42.
[92] Yakunin S, Protesescu L, Krieg F, et al. Low-threshold amplified spontaneous emission and lasing from colloidal nanocrystals of caesium lead halide perovskites. Nat Commun 2015;6:8056.
[93] Ioppolo T, Stubblefield J, Ötügen MV. Electric field-induced deformation of polydimethylsiloxane polymers. J Appl Phys 2012;112:044906.
[94] Weng WL, Anstie JD, Stace TM, Campbell G, Baynes FN, Luiten AN. Nano-Kelvin thermometry and temperature control: beyond the thermal noise limit. Phys Rev Lett 2014;112:160801.
[95] Kippenberg TJ, Vahala KJ. Cavity opto-mechanics. Opt Express 2007;15:17172–205.
[96] Yu W, Jiang WC, Lin Q, Lu T. Cavity optomechanical spring sensing of single molecules. Nat Commun 2016;7:12311.
[97] Dahan R, Martin LL, Carmon T. Droplet optomechanics. Optica 2016;3:175–8.
[98] Gavartin E, Verlot P, Kippenberg TJ. A hybrid on-chip optomechanical transducer for ultrasensitive force measurements. Nat Nanotechnol 2012;7:509–14.
[99] Wang CY, Herr T, Del'Haye P, et al. Mid-infrared optical frequency combs at 2.5 μm based on crystalline microresonators. Nat Commun 2013;4:1345.
[100] Roelli P, Galland C, Piro N, Kippenberg TJ. Molecular cavity optomechanics as a theory of plasmon-enhanced Raman scattering. Nat Nanotechnol 2016;11:164–9.
[101] Schmidt MK, Esteban R, Gonzalez-Tudela A, Giedke G, Aizpurua J. Quantum mechanical description of Raman scattering from molecules in plasmonic cavities. ACS Nano 2016;10:6291–8.
[102] Teraoka I, Arnold S. Theory of resonance shifts in TE and TM whispering gallery modes by nonradial perturbations for sensing application. J Opt Soc Am B: Opt Phys 2006;23:1381–9.
[103] Foreman MR, Vollmer F. Theory of resonance shifts of whispering gallery modes by arbitrary plasmonic nanoparticles. New J Phys 2013;15:083006.
[104] Foreman MR, Vollmer F. Level repulsion in hybrid photonic-plasmonic microresonators for enhanced biodetection. Phys Rev A 2013;88:023831.
[105] Santiago-Cordoba MA, Boriskina SV, Vollmer F, Demirel MC. Nanoparticle-based protein detection by optical shift of a resonant microcavity. Appl Phys Lett 2011;99:073701.
[106] Swaim JD, Knittel J, Bowen WP. Detection limits in whispering gallery biosensors with plasmonic enhancement. Appl Phys Lett 2011;99:243109.
[107] Shopova SI, Rajmangal R, Holler S, Arnold S. Plasmonic enhancement of a whispering-gallery-mode biosensor for single nanoparticle detection. Appl Phys Lett 2011;98:243104.
[108] Santiago-Cordoba MA, Cetinkaya M, Boriskina SV, Vollmer F, Demirel MC. Ultrasensitive detection of a protein by optical trapping in a photonic-plasmonic microcavity. J Biophotonics 2012;5:629–38.
[109] Baaske MD, Vollmer F. Optical observation of single atomic ions interacting with plasmonic nanorods in aqueous solution. Nat Photonics 2016;10:733–9.
[110] Kim E, Baaske MD, Vollmer F. In situ observation of single-molecule surface reactions from low to high affinities. Adv Mater 2016;28:9941–8.
[111] Min BK, Ostby E, Sorger V, et al. High-Q surface-plasmon-polariton whispering-gallery microcavity. Nature 2009;457:455–8.
[112] Arbabi E, Kamali SM, Arnold S, Goddard LL. Hybrid whispering gallery mode/plasmonic chain ring resonators for biosensing. Appl Phys Lett 2014;105:231107.
[113] Heylman KD, Thakkar N, Horak EH, et al. Optical microresonators as single-particle absorption spectrometers. Nat Photonics 2016;10:788–95.
[114] Zhang Y, Zhen Y-R, Neumann O, Day JK, Nordlander P, Halas NJ. Coherent anti-Stokes Raman scattering with single-molecule sensitivity using a plasmonic Fano resonance. Nat Commun 2014;5:4424.
[115] Kim E, Baaske MD, Schuldes I, Wilsch PS, Vollmer F. Label-free optical detection of single enzyme-reactant reactions and associated conformational changes. Sci Adv 2017;3:e1603044.
[116] Notomi M. Manipulating light with strongly modulated photonic crystals. Rep Prog Phys 2010;73:096501.
[117] Strutt JW. On the maintenance of vibrations by forces of double frequency, and on the propagation of waves through a medium endowed with a periodic structure. Phil Mag 1887;24:145–59.

[118] Bykov VP. Spontaneous emission in a periodic structure. Sov Phys JETP 1972;35:269–73.
[119] Ohtaka K. Energy band of photons and low-energy photon diffraction. Phys Rev B 1979;19:5057–67.
[120] Yablonovitch E. Inhibited spontaneous emission in solid-state physics and electronics. Phys Rev Lett 1987;58:2059–62.
[121] John S. Strong localization of photons in certain disordered dielectric superlattices. Phys Rev Lett 1987;58:2486–9.
[122] Joannopoulos JD, Johnson SG, Winn JN, Meade RD. Photonic crystals: molding the flow of light, 2nd ed. Princeton: Princeton University Press, 2008.
[123] Zhuo Y, Cunningham BT. Label-free biosensor imaging on photonic crystal surfaces. Sensors 2015;15:21613–35.
[124] Cunningham BT, Zhang M, Zhuo Y, Kwon L, Race C. Recent advances in biosensing with photonic crystal surfaces: a review. IEEE Sens J 2016;16:3349–66.
[125] Inan H, Poyraz M, Inci F, et al. Photonic crystals: emerging biosensors and their promise for point-of-care applications. Chem Soc Rev 2017;46:366–88.
[126] Baker JE, Sriram R, Miller BL. Two-dimensional photonic crystals for sensitive microscale chemical and biochemical sensing. Lab Chip 2015;15:971–90.
[127] Zhang YN, Zhao Y, Lv RQ. A review for optical sensors based on photonic crystal cavities. Sens Actuators, A 2015;233:374–89.
[128] Notomi M. Manipulating light by photonic crystals. NTT Tech Rev 2009;7:1–10.
[129] Johnson SG, Villeneuve PR, Fan SH, Joannopoulos JD. Linear waveguides in photonic-crystal slabs. Phys Rev B 2000;62:8212–22.
[130] Topolancik J, Vollmer F, Ilic R, Crescimanno M. Out-of-plane scattering from vertically asymmetric photonic crystal slab waveguides with in-plane disorder. Opt Express 2009;17:12470–80.
[131] Topolancik J, Ilic B, Vollmer F. Experimental observation of strong photon localization in disordered photonic crystal waveguides. Phys Rev Lett 2007;99:253901.
[132] Sapienza L, Thyrrestrup H, Stobbe S, Garcia PD, Smolka S, Lodahl P. Cavity quantum electrodynamics with Anderson-localized modes. Science 2010;327:1352–5.
[133] Javadi A, Maibom S, Sapienza L, Thyrrestrup H, García PD, Lodahl P. Statistical measurements of quantum emitters coupled to Anderson-localized modes in disordered photonic-crystal waveguides. Opt Express 2014;22:30992–1001.
[134] Asano T, Ochi Y, Takahashi Y, Kishimoto K, Noda S. Photonic crystal nanocavity with a Q factor exceeding eleven million. Opt Express 2017;25:1769–77.
[135] Threm D, Nazirizadeh Y, Gerken M. Photonic crystal biosensors towards on-chip integration. J Biophotonics 2012;5:601–16.
[136] Skivesen N, Têtu A, Kristensen M, Kjems J, Frandsen LH, Borel PI. Photonic-crystal waveguide biosensor. Opt Express 2007;15:3169–76.
[137] Lee M, Fauchet PM. Two-dimensional silicon photonic crystal based biosensing platform for protein detection. Opt Express 2007;15:4530–5.
[138] Dorfner D, Zabel T, Hürlimann T, et al. Photonic crystal nanostructures for optical biosensing applications. Biosens Bioelectron 2009;24:3688–92.
[139] Kita S, Otsuka S, Hachuda S, et al. Photonic crystal nanolaser biosensors. IEICE Trans Electron 2012;E95C:188–98.
[140] Chen YF, Serey X, Sarkar R, Chen P, Erickson D. Controlled photonic manipulation of proteins and other nanomaterials. Nano Lett 2012;12:1633–7.
[141] Scullion MG, Krauss TF, Di Falco A. Slotted photonic crystal sensors. Sensors 2013;13:3675–710.
[142] Zou Y, Chakravarty S, Kwong DN, et al. Cavity-waveguide coupling engineered high sensitivity silicon photonic crystal microcavity biosensors with high yield. IEEE J Sel Top Quantum Electron 2014;20:6900710.
[143] Zlatanovic S, Mirkarimi LW, Sigalas MM, et al. Photonic crystal microcavity sensor for ultracompact monitoring of reaction kinetics and protein concentration. Sens Actuators 2009;B141:13–9.
[144] Toccafondo V, García-Rupérez J, Bañuls MJ, et al. Single-strand DNA detection using a planar photonic-crystal-waveguide-based sensor. Opt Lett 2010;35:3673–5.
[145] van Leest T, Caro J. Cavity-enhanced optical trapping of bacteria using a silicon photonic crystal. Lab Chip 2013;13:4358–65.
[146] Tardif M, Jager JB, Marcoux PR, et al. Single-cell bacterium identification with a SOI optical microcavity. Appl Phys Lett 2016;109:133510.
[147] Chakravarty S, Lai WC, Zou Y, et al. Multiplexed specific label-free detection of NCI-H358 lung cancer cell line lysates with silicon based photonic crystal microcavity biosensors. Biosens Bioelectron 2013;43:50–5.
[148] Pal S, Yadav AR, Lifson MA, Baker JE, Fauchet PM, Miller BL. Selective virus detection in complex sample matrices with photonic crystal optical cavities. Biosens Bioelectron 2013;44:229–234.
[149] Baker JE, Sriram R, Miller BL. Recognition-mediated particle detection under microfluidic flow with waveguide-coupled 2D photonic crystals: towards integrated photonic virus detectors. Lab Chip 2017;17:1570–7.
[150] Kang P, Schein P, Serey X, O'Dell D, Erickson D. Nanophotonic detection of freely interacting molecules on a single influenza virus. Sci Rep 2015;5:12087.
[151] Di Falco A, O'Faolain L, Krauss TF. Chemical sensing in slotted photonic crystal heterostructure cavities. Appl Phys Lett 2009;94:063503.
[152] Safavi-Naeini AH, Alegre TPM, Winger M, Painter O. Optomechanics in an ultrahigh-Q two-dimensional photonic crystal cavity. Appl Phys Lett 2010;97:181106.
[153] Scullion MG, Di Falco A, Krauss TF. Slotted photonic crystal cavities with integrated microfluidics for biosensing applications. Biosens Bioelectron 2011;27:101–5.
[154] Shambat G, Kothapalli SR, Provine J, et al. Single-cell photonic nanocavity probes. Nano Lett 2013;13:4999–5005.
[155] Lu TW, Lee PT. Photonic crystal nanofishbone nanocavity. Opt Lett 2013;38:3129–32.
[156] Liang F, Clarke N, Patel P, Loncar M, Quan QM. Scalable photonic crystal chips for high sensitivity protein detection. Opt Express 2013;21:32306–12.
[157] Serey X, Mandal S, Erickson D. Comparison of silicon photonic crystal resonator designs for optical trapping of nanomaterials. Nanotechnology 2010;21:305202.
[158] Chen Y, Fegadolli WS, Jones WM, Scherer A, Li M. Ultrasensitive gas-phase chemical sensing based on functionalized photonic crystal nanobeam cavities. ACS Nano 2014;8:522–7.

[159] Lin T, Zhang XW, Zhou GY, Siong CF, Deng J. Design of an ultra-compact slotted photonic crystal nanobeam cavity for biosensing. J Opt Soc Am B: Opt Phys 2015;32:1788–91.
[160] Liang F, Quan Q. Detecting single gold nanoparticles (1.8 nm; with ultrahigh-Q air-mode photonic crystal nanobeam cavities. ACS Photonics 2015;2:1692–7.
[161] Lin SY, Hu JJ, Kimerling L, Crozier K. Design of nanoslotted photonic crystal waveguide cavities for single nanoparticle trapping and detection. Opt Lett 2009;34:3451–3.
[162] Baba T, Kita S, Abe H, et al. Photonic crystal nanolasers with nanoslot structure for sensing applications. Proc. SPIE 8095, Active Photonic Materials IV, 80950X (September 12, 2011).
[163] Kita S, Hachuda S, Otsuka S, et al. Super-sensitivity in label-free protein sensing using a nanoslot nanolaser. Opt Express 2011;19:17683–90.
[164] Hachuda S, Otsuka S, Kita S, et al. Selective detection of sub-atto-molar Streptavidin in 10^{13}-fold impure sample using photonic crystal nanolaser sensors. Opt Express 2013;21:12815–21.
[165] Baba T. Biosensing using photonic crystal nanolasers. MRS Commun 2015;5:555–64.
[166] Takahashi D, Hachuda S, Watanabe T, Nishijima Y, Baba T. Detection of endotoxin using a photonic crystal nanolaser. Appl Phys Lett 2015;106:131112.
[167] Abe H, Narimatsu M, Watanabe T, et al. Living-cell imaging using a photonic crystal nanolaser array. Opt Express 2015;23:17056–66.
[168] Hachuda S, Watanabe T, Takahashi D, Baba T. Sensitive and selective detection of prostate-specific antigen using a photonic crystal nanolaser. Opt Express 2016;24:12886–92.
[169] Skorobogatiy M, Kabashin AV. Photon crystal waveguide-based surface plasmon resonance biosensor. Appl Phys Lett 2006;89:143518.
[170] De Angelis F, Patrini M, Das G, et al. A hybrid plasmonic-photonic nanodevice for label-free detection of a few molecules. Nano Lett 2008;8:2321–7.
[171] De Angelis F, Das G, Candeloro P, et al. Nanoscale chemical mapping using three-dimensional adiabatic compression of surface plasmon polaritons. Nat Nanotechnol 2010;5:67–72.
[172] Lin SY, Zhu WQ, Jin YH, Crozier KB. Surface-enhanced Raman scattering with Ag nanoparticles optically trapped by a photonic crystal cavity. Nano Lett 2013;13:559–63.
[173] Ciminelli C, Conteduca D, Dell'Olio F, Armenise MN. Design of an optical trapping device based on an ultra-high Q/V resonant structure. IEEE Photonics J 2014;6:0600916.
[174] Zhuo Y, Hu H, Chen WL, et al. Single nanoparticle detection using photonic crystal enhanced microscopy. Analyst 2014;139:1007–15.
[175] Aristov AI, Manousidaki M, Danilov A, et al. 3D plasmonic crystal metamaterials for ultra-sensitive biosensing. Sci Rep 2016;6:25380.
[176] Sediq KN, Coles D, Fry PW, Lidzey DG. Plasmonic gold nanodiscs fabricated into a photonic-crystal nanocavity. Nanotechnology 2016;27:225203.
[177] Kelaita YA, Fischer KA, Babinec TM, et al. Hybrid metal-dielectric nanocavity for enhanced light-matter interactions. Opt Mater Express 2017;7:231–9.
[178] Liu C, Wang Z, Li EW, et al. Electrokinetic manipulation integrated plasmonic photonic hybrid Raman nanosensors with dually enhanced sensitivity. ACS Sensors 2017;2:346–53.
[179] Zhang TP, Callard S, Jamois C, Chevalier C, Feng D, Belarouci A. Plasmonic-photonic crystal coupled nanolaser. Nanotechnology 2014;25:315201.
[180] Kong XM, Xi YT, LeDuff P, et al. Optofluidic sensing from inkjet-printed droplets: the enormous enhancement by evaporation-induced spontaneous flow on photonic crystal biosilica. Nanoscale 2016;8:17285–94.
[181] Kong XM, Xi YT, Le Duff P, et al. Detecting explosive molecules from nanoliter solution: a new paradigm of SERS sensing on hydrophilic photonic crystal biosilica. Biosens Bioelectron 2017;88:63–70.
[182] Liang F, Guo Y, Hou S, Quan Q. Photonic-plasmonic hybrid single-molecule nanosensor measures the effect of fluorescent labels on DNA-protein dynamics. Sci Adv 2017;3:e1602991.
[183] Chakravarty S, Chen XN, Tang NM, et al. Review of design principles of 2D photonic crystal microcavity biosensors in silicon and their applications. Front Optoelectron 2016;9:206–24.
[184] Yang CJ, Tang NM, Yan H, Chakravarty SS, Li DH, Chen RT. 193nm lithography fabricated high sensitivity photonic crystal microcavity biosensors for plasma protein detection in patients with pancreatic cancer. CLEO: 2015, OSA Technical Digest online (Optical Society of America, San Jose, CA, USA, 2015), paper STu4K.5.
[185] Chakravarty S, Hosseini A, Xu XC, Zhu L, Zou Y, Chen RT. Analysis of ultra-high sensitivity configuration in chip-integrated photonic crystal microcavity bio-sensors. Appl Phys Lett 2014;104:191109.
[186] Xu XC, Subbaraman H, Chakravarty S, et al. Flexible single-crystal silicon nanomembrane photonic crystal cavity. ACS Nano 2014;8:12265–71.
[187] Zou Y, Chakravarty S, Zhu L, Chen RT. The role of group index engineering in series-connected photonic crystal microcavities for high density sensor microarrays. Appl Phys Lett 2014;104:141103.
[188] Lee MR, Fauchet PM. Nanoscale microcavity sensor for single particle detection. Opt Lett 2007;32:3284–6.
[189] Painter O, Lee RK, Scherer A, et al. Two-dimensional photonic band-gap defect mode laser. Science 1999;284:1819–21.
[190] Nozaki K, Kita S, Baba T. Room temperature continuous wave operation and controlled spontaneous emission in ultrasmall photonic crystal nanolaser. Opt Express 2007;15:7506–14.
[191] Lončar M, Scherer A, Qiu YM. Photonic crystal laser sources for chemical detection. Appl Phys Lett 2003;82:4648–50.
[192] Kita S, Hachuda S, Nozaki K, Baba T. Nanoslot laser. Appl Phys Lett 2010;97:161108.
[193] Watanabe T, Abe H, Nishijima Y, Baba T. Array integration of thousands of photonic crystal nanolasers. Appl Phys Lett 2014;104:121108.
[194] Velha P, Rodier JC, Lalanne P, et al. Ultracompact silicon-on-insulator ridge-waveguide mirrors with high reflectance. Appl Phys Lett 2006;89:171121.
[195] Quan QM, Loncar M. Deterministic design of wavelength scale, ultra-high Q photonic crystal nanobeam cavities. Opt Express 2011;19:18529–42.
[196] Yang XD, Ishikawa A, Yin XB, Zhang X. Hybrid photonic-plasmonic crystal nanocavities. ACS Nano 2011;5:2831–8.

[197] Woldering LA, Mosk AP, Vos WL. Design of a three-dimensional photonic band gap cavity in a diamondlike inverse woodpile photonic crystal. Phys Rev B 2014;90:115140.
[198] Bodelon G, Montes-Garcia V, Lopez-Puente V, et al. Detection and imaging of quorum sensing in Pseudomonas aeruginosa biofilm communities by surface-enhanced resonance Raman scattering. Nat Mater 2016;15:1203–11.
[199] Yang SK, Dai XM, Stogin BB, Wong TS. Ultrasensitive surface-enhanced Raman scattering detection in common fluids. Proc Natl Acad Sci USA 2016;113:268–73.